CHD-associated enhancers shape human cardiomyocyte lineage commitment

Daniel A. Armendariz[1,*], Sean C. Goetsch[2,*], Anjana Sundarrajan[1], Sushama Sivakumar[2], Yihan Wang[1], Shiqi Xie[1], Nikhil Munshi[2,3,4,#], Gary C. Hon[1,4,5,#,^]

[1]Cecil H. and Ida Green Center for Reproductive Biology Sciences, University of Texas Southwestern Medical Center, Dallas, TX 75390, USA

[2]Department of Internal Medicine, University of Texas Southwestern Medical Center, Dallas, TX 75390, USA

[3]Division of Cardiology, Department of Molecular Biology, McDermott Center for Human Growth and Development, University of Texas Southwestern Medical Center, Dallas, TX 75390, USA

[4]Hamon Center for Regenerative Science and Medicine, University of Texas Southwestern Medical Center, Dallas, TX 75390, USA

[5]Lyda Hill Department of Bioinformatics, Department of Obstetrics and Gynecology, University of Texas Southwestern Medical Center, Dallas, TX 75390, USA

*These authors contributed equally.

^Lead contact

#Correspondence to: Nikhil.Munshi@utsouthwestern.edu and Gary.Hon@utsouthwestern.edu

ABSTRACT

Enhancers orchestrate gene expression programs that drive multicellular development and lineage commitment. Thus, genetic variants at enhancers are thought to contribute to developmental diseases by altering cell fate commitment. However, while many variant-containing enhancers have been identified, studies to endogenously test the impact of these enhancers on lineage commitment have been lacking. We perform a single-cell CRISPRi screen to assess the endogenous roles of 25 enhancers and putative cardiac target genes implicated in genetic studies of congenital heart defects (CHD). We identify 16 enhancers whose repression leads to deficient differentiation of human cardiomyocytes (CMs). A focused CRISPRi validation screen shows that repression of TBX5 enhancers delays the transcriptional switch from mid- to late-stage CM states. Endogenous genetic deletions of two TBX5 enhancers phenocopy epigenetic perturbations. Together, these results identify critical enhancers of cardiac development and suggest that misregulation of these enhancers could contribute to cardiac defects in human patients.

HIGHLIGHTS:

- Single-cell enhancer perturbation screens during human cardiomyocyte differentiation.
- Perturbation of CHD-linked enhancers/genes causes deficient CM differentiation.
- Repression or knockout of TBX5 enhancers delays transition from mid to late CM states.
- Deficient differentiation coincides with reduced expression of known cardiac genes.

INTRODUCTION

Congenital heart defects (CHD) encompass a broad range of cardiac malformations that impact 1% of all births (Hoffman and Kaplan, 2002). However, the genetic basis for 54% of familial and 80% of sporadic CHD cases remain unknown (Blue et al., 2017). Genome-wide association studies and whole genome sequencing of CHD patients have identified thousands of variants that associate with CHD (Agopian et al., 2017; Cordell et al., 2013; Richter et al., 2020). Most efforts have focused on functionally characterizing coding variants. For example, traditional linkage analysis in patients with Holt-Oram Syndrome implicated the gene for the TBX5 transcription factor, which harbors variants predicted to disrupt protein structure and/or function in affected patients (Basson et al., 1997).

TBX5 is a key regulator of cardiac development, which requires precise temporal expression: early expression of TBX5 is necessary for cardiomyocyte maturation and later expression is required for specification of the cardiac conduction system (Bruneau et al., 2001; Steimle and Moskowitz, 2017). However, protein-coding variants account for only a small fraction of CHD risk. In contrast, the vast majority of de novo variants are non-coding and potentially modify the activity of transcriptional enhancers (Richter et al., 2020). Only a handful have been functionally examined, including a non-coding CHD-associated variant which has been shown to impair proper TBX5 expression (Smemo et al., 2012). Thus, there remains a critical gap in knowledge between CHD-associated non-coding regions and their contribution to CHD.

Recent studies have explored high throughput genomic approaches to assess the roles of enhancers and regulatory variants. For example, Richter et al. performed whole genome sequencing in CHD patients to identify thousands of non-coding variants (Richter et al., 2020). Following extensive computational filtering to narrow the list of putative causal mutations, the authors used massively parallel reporter assays to functionally identify 5 CHD-associated variants that impact enhancer activity. However, reporter assays do not assess how variants function in the endogenous genomic context. CRISPR screens have been developed to identify regulatory elements that contribute to screenable phenotypes following epigenetic silencing or genetic deletion (Fulco et al., 2016). While powerful, this strategy has focused on screenable phenotypes in homogeneous cell populations. Thus, traditional CRISPR screens would lose information about how enhancers regulate specification of distinct cell types during development.

To address this deficiency, single-cell approaches have been applied in isogenic systems to delineate how perturbations affect lineage commitment. For example, Kathiriya et al generated an allelic series of TBX5 locus modifications in iPSCs followed by CM differentiation and single-cell sequencing to show that TBX5 exhibits a dosage sensitive effect altering the trajectory of CM specification (Kathiriya et al., 2021). Recent studies have extended this approach using single-cell CRISPR screens to systematically test the roles of key genes in endoderm and neuronal specification (Genga et al., 2019; Tian et al., 2019). Similar approaches have also been applied for high throughput examination of enhancer functions in stable, homogeneous cell lines like K562 cells (Gasperini et al., 2019; Xie et al., 2017). A combination of these approaches will likely be required to systematically study the endogenous functions of CHD-associated enhancers during CM lineage commitment.

Here, we apply a single-cell CRISPRi screen for 25 CHD-associated enhancers in a model of hESC to CM differentiation. We identify a subset of 16 enhancers which, when perturbed, results in deficient CM specification. In focused validation studies, we show that CRISPRi repression or genetic deletion of TBX5 enhancers leads to dysregulation of the cardiac gene

expression program, enrichment of early CM cell states, and a depletion of mature CM cell states.

RESULTS

Single-cell screens of CHD-associated enhancers during cardiomyocyte differentiation

Whole genome sequencing has identified >50,000 de novo variants in 749 CHD patients (Richter et al., 2020). Some of these variants may contribute to CHD by modulating the activity of transcriptional enhancers that are active in cardiac development. To identify these enhancers for functional study, we overlapped variants with published epigenetic datasets of active enhancers including open chromatin (ATAC-Seq) and histone acetylation (H3K27ac) (Liu et al., 2017; Zhang et al., 2019). We prioritized a diverse set of CHDs from atrial and septal defects to Tetralogy of Fallot (**Table S1**). We also filtered for enhancers within 100-kb of genes with known roles in heart development. Overall, we prioritized 25 enhancers, including those in proximity to known cardiac regulators, with many exhibiting high predicted sequence conservation (van den Hoogenhof et al., 2018; Siepel et al., 2005) (**Figure 1A**). Epigenetic evidence indicates that many of these enhancers and their putative downstream genes become active at early time points of cardiac differentiation (Tompkins et al., 2016) (**Figure 1B-C)**. Overall, these data suggest that the prioritized CHD-associated enhancers may have roles in early cardiac lineage commitment, and we hypothesize that perturbations of these enhancers may impact cell fate.

To test this hypothesis, we used CRISPRi-mediated single-cell perturbation screens to assess the functions of CHD-associated enhancers during early cardiac lineage commitment (**Supplemental Figure S1A-B**). We modeled this process by differentiating human embryonic stem cells (hESCs) towards cardiomyocytes through WNT modulation. Notably, to preserve cellular heterogeneity, we performed CM differentiation without metabolic selection (Tohyama et al., 2013). To capture the early events of lineage commitment, we examined cells at day 8 of differentiation (**Figure 1D**). Overall, we targeted 397 sgRNAs spanning 25 enhancers, 19 promoters of their putative target genes, and non-genome targeting controls (NT) (**Table S1**). After single-cell RNA sequencing and stringent filtering to remove low-quality cells and doublets, we retained 80,343 high-quality cells for downstream analysis. On average, we detected 1 sgRNA in each cell (**Supplemental Figure S1C-E and Table S2**).

To define the cell populations during early differentiation, we clustered cells to identify 7 distinct cell populations across all 3 germ layers (**Figure 1E and Table S3**). We focused on the 3 mesoderm derived clusters due to their relevance to cardiac development. These clusters included TNNT2+ cardiomyocytes, FN1+ mesodermal cells (Cheng et al., 2013), and COL3A1+ cardiac fibroblasts (van Nieuwenhoven et al., 2013) (**Figure 1F and Supplemental Figure S1F**). Verifying the efficiency of CRISPRi mediated repression, we observed robust depletion of control genes for positive control sgRNAs (p_{Malat1} < 2.2e-308, Mann-Whitney U) (**Figure 1G and Supplemental Figure S1G**).

CRISPRi of CHD-associated enhancers delays cardiomyocyte differentiation

To test the ability of our approach to detect changes in cell state from CRISPRi perturbations, we included positive control sgRNAs targeting the promoter of well-known cardiac genes as an internal quality control measure. We first examined sgRNAs targeting the promoter of ZIC2, a known regulator of both neuronal and cardiac lineages necessary for the successful

differentiation of both (Luo et al., 2015; Xu et al., 2020). Compared to cells with non-target sgRNAs, the cells containing sgRNAs for ZIC2 promoter were significantly depleted for neuronal and cardiac populations ($p_{neuronal}$ = 4.7e-61; $p_{cardiomyocytes}$ = 1.9e-5, hypergeometric test). Consistent with a stalled differentiation state, these cells exhibit enrichment for an early mesodermal state (**Supplemental Figure S1H**). Second, based on published knockout studies showing that TBX5 repression prevents proper CM specification (Kathiriya et al., 2021), we also included sgRNAs targeting the promoter of TBX5. We observed that loss of TBX5 expression led to a depletion in CMs ($p_{TBX5\ promoter}$ = 2.0e-5; $p_{TBX5\ enhancer\ 6}$ = 0.025, hypergeometric test) and a corresponding increase in early mesoderm cells ($p_{TBX5\ promoter}$ = 3.4e-11; $p_{TBX5\ Enhancer\ 6}$ = 4.1e-4, hypergeometric test) (**Figure 1H**). Interestingly, perturbation of a CHD-associated enhancer of TBX5 phenocopies perturbation of the promoter in terms of cell state changes. Bulk qPCR analysis confirms that CRISPRi of TBX5 enhancers results in loss of TBX5 expression (**Supplemental Figure S1I**). Taken together, this analysis demonstrates that CRISPRi repression at the TBX5 promoter functions as expected during CM differentiation and suggests further that repression of TBX5 expression through enhancer perturbation similarly depletes CM lineage commitment through loss of downstream target expression.

Next, to gain higher resolution insights on how enhancer perturbation influences lineage commitment, we focused on cells in the cardiac lineage (CM, mesoderm). We identified a trajectory of differentiating cardiomyocytes composed of 4 distinct subpopulations including SOX4+ progenitors (Paul et al., 2014), FN1+ early-stage CMs, ACTA2+ mid-stage CMs (Potta et al., 2010), and NPPA+ atrial-like late-stage CMs (**Figure 2A and Supplemental Figure S2A)**. Consistent with the established process of CM commitment, pseudotime analysis orders these cell states with increasing expression of cardiac maturation genes such as TNNT2 (**Figure 2B-C**). Further validating this trajectory, we observe consistency with published bulk RNA-seq datasets of CM differentiation (Tompkins et al., 2016)(**Figure 2D**). Thus, our single-cell dataset recapitulates the expected patterns of CM cell fate commitment.

A previous study established that loss of cardiogenic TFs deviates cells from a WT trajectory (Kathiriya et al., 2021). To examine the effect of enhancers, we compared the cell state distribution in perturbed cells. Surprisingly, we observed that perturbation of 16 enhancers led to a depletion of late stage CMs. In contrast, only 2 enhancers were depleted in earlier CM states. This depletion of late-stage CMs coincides with an enrichment in progenitor, early CM, and mid CM states (**Figure 2E and Supplemental Figure S2B-C**). Since connecting enhancers with their cognate promoters can be challenging, we only considered enhancer perturbations that produced phenotypes similar to paired promoter perturbation. Using this stringent approach, we detected 14 out of 25 enhancer perturbations that caused changes in cell state distribution, although this likely represents an underestimate of the true hit rate. To account for the low expression of many cardiac genes which makes differential gene expression analysis underpowered, we performed targeted sequencing to measure the expression of key cardiac gene targets (**Figure S2D**). This analysis showed further consistency between promoter-targeting and enhancer-targeting sgRNAs (**Figure S2E**).

Next, we illustrate several examples. First, we targeted two evolutionarily conserved enhancers near the CM structural protein TNNT2 that exhibit active enhancer chromatin during CM differentiation (**Figure 2F**). We observed that CRISPRi repression of either the TNNT2 promoter or one of the two targeted nearby enhancers resulted in a depletion of late CM cells ($p_{TNNT2\ P1}$ = 0.0005; $p_{TNNT2\ E2}$ = 0.03; $p_{TNNT2\ E3}$ = 0.001, hypergeometric test) (**Figure 2G**). These perturbations also yielded similar changes in pseudotime cell state along with reduced expression of TNNT2 and other cardiac genes within the CM populations ($p_{TNNT2\ P1}$ = 0.0004; $p_{TNNT2\ E2}$ = 0.07; $p_{TNNT2\ E3}$ = 1.2e-6, Mann-Whitney U) (**Figure 2H-2I and Table S4**). Second, we also targeted a

CHD-associated enhancer with a variant characterized by reporter assay analysis (Gilsbach et al., 2018; Richter et al., 2020) (**Figure 2J**). Repression of this enhancer also impacted lineage specification, depleting cells in the late CM state (p = 2.5e-5, hypergeometric test) (p = 3.6e-5,Mann-Whitney U) (**Figure 2K-2L**). Third, we examined how perturbation of 6 distinct TBX5 enhancers affected CM trajectory. CRISPRi-mediated repression of any of the 6 TBX5 enhancers led to a depletion of late CM ($p_{Enhancers1-6}$ between 3.7e-2 and 1.9e-8, hypergeometric test) ($p_{Enhancers1-6}$ between 2.5e-2 and 6.8e-9, Mann-Whitney U) (**Figure 2E,M-N**). Cells with sgRNAs targeting TBX5 enhancers showed reduced expression TBX5 downstream targets, including NPPA and NPPB (**Figure 2O and Table S4**) (Houweling et al., 2005). Consistently, we also observed changes in cell state upon repression of TBX5 promoters. In sum, we observe that perturbation of CHD-associated enhancers, particularly for TBX5, results in deficient CM differentiation. These results suggest that these enhancers have roles in CM lineage commitment.

A focused validation screen demonstrates that TBX5 enhancers modulate CM cell fate

To validate the results of the large screen above, we performed a smaller single-cell CRISPRi screen focused on TBX5 regulatory elements. Three of the enhancers (Enh4, Enh5, and Enh6), were previously identified through sequence conservation and exhibited reporter activity (Smemo et al., 2012). The remaining three enhancers (Enh1, Enh2, Enh3), were identified in this study based on epigenetic hallmarks of active enhancers (**Figure 3A**). After transduction of control and targeting sgRNAs, CM differentiation, and sequencing, we identified 3 primary clusters comprising all germ layers (**Figure 3B, Supplemental Figure S3A, and Table S3**), with 3,102 cells corresponding to CMs based on TNNT2 expression (**Figure 3C**).

Consistent with our initial screen, we observed that cells with TBX5 enhancer repression were significantly depleted in the late CM state ($p_{Enhancers1-6}$ between 1.3e-5 and 1.3e-19, hypergeometric test) (**Figure 3D-E and Supplemental Figure S3B**). We also observed activation of ACTA2 and repression of NPPA in cells with perturbed TBX5 enhancers (p_{ACTA2} = 3.1e-7; p_{NPPA} = 8.2e-24, Mann-Whitney U) (**Figure 3F, Supplemental Figure S3C, and Table S4**), consistent with a previous study that knocked out TBX5 (Kathiriya et al., 2021).

Next, we performed focused analysis on CM populations to identify 3 clusters of cell subpopulations: CM progenitors (FN1+), mid CM (ACTA2+), and late CM (NPPA+) (**Figure 4A and Supplemental Figure S4A**). Pseudotime analysis orders these cell populations by increasing expression of known cardiac maturation genes including NPPA and TNNT2 (**Figure 4B-4D**). Overall, our focused screen contains 122 cells balanced across TBX5 enhancer perturbations that attain CM states. Since this number is relatively small, we pooled these cells for downstream analyses. Consistent with our larger screen, we observe a significant depletion of late CMs when TBX5 enhancers are repressed, with an increase in mid CMs (**Figure 4E-4F and Supplemental Figure S4B**) and a significant decrease in pseudotime rank ($p_{Late\ CM}$ = 3.8e-18; $p_{Mid\ CM}$ = 7.8e-13, hypergeometric test) (p = 2.2e-5, Mann-Whitney U) (**Figure 4G**). This coincided with downregulation of known targets of TBX5 (**Supplemental Figure S4C and Table S4**). Cell label transfer of initial screen CM annotations onto focus screen CMs showed consistent clustering and retention of late CM depletion under TBX5 enhancer knockdown conditions (**Supplemental Figure S4D-S4E**). Overall, results from our focused validation screen are consistent with the observation that TBX5 enhancer repression causes deficient CM lineage commitment.

TBX5 enhancer repression alters CM molecular signatures

While TBX5 enhancer perturbation results in a reduction of late CM cells, we observe that a small number of cells still reach the state. We next asked whether these cells exhibit altered molecular signatures. First, focusing on the late CM state, we defined 80 genes that are specifically expressed in NT control cells. These genes coincide with expected CM markers, such as NPPA and TTN, which continuously increase in expression throughout CM differentiation. Interestingly, we find that this set of late-CM genes is depleted in the subset of cells with perturbed TBX5 enhancers (denoted sgTBX5enh) that reach the late-CM state (p = 1.7e-3, z-test) (**Figure 4H-4I and Table S5**). Several notable cardiac genes including NPPA and NPPB exhibit pronounced repression in perturbed cells (**Figure 4J-K**). These observations suggest that, although some sgTBX5Enh cells can reach a late-CM cell state, these cells have deficient activation of late-CM genes. We next asked if these cells also harbored aberrant expression of mid-CM cell signatures.

We identified a set of 18 genes that define the mid-CM state, which includes the structural proteins MYL4 and MYL6. Pseudotime analysis shows that NT control cells repress mid-CM genes as they enter the late-CM stage (**Figure 4L**). In contrast, we observe that sgTBX5Enh cells retain higher expression levels of mid-CM genes in the late-CM state (p = 2.6e-4, z-test) (**Figure 4M and Table S5**). For example, perturbed cells have a 48% increase in HAS2 expression compared to NT control cells ($p_{Progenitor}$ = 0.064; $p_{Mid\ CM}$ = 0.0006; $p_{Late\ CM}$ = 0.1, Mann-Whitney U) (**Figure 4N-O**).

In summary, we observe that perturbed cells express late-CM genes at lower levels and mid-CM genes at higher levels than NT control cells in the late-CM state. This suggests that although a subset of sgTBX5Enh cells can reach the late-CM cell state, these cells are in a delayed differentiation state that reflects mid-CM gene signatures. Taken together with previous observations, misregulation of TBX5 through enhancer modulation leads to deficient induction of CM transcriptional signatures that are associated with CM fate commitment.

TBX5 enhancer knockouts recapitulate cardiac phenotypes

Next, to confirm the results from the CRISPRi experiments above, we used a CRISPR/Cas9 strategy to genetically delete enhancers. We focused on the two TBX5 enhancers (Enh3 and Enh5) that harbor CHD-associated variants and exhibit the strongest cellular phenotypes in the CRISPRi screens. To compare enhancer deletion to gene deletion, we also knocked out TBX5 exon 3 (Kathiriya et al., 2021). We screened, isolated, and confirmed clones with biallelic deletion of either Enh3 (TBX5Enh3$^{-/-}$), Enh5 (TBX5Enh5$^{-/-}$), or Exon 3 (TBX5Exon$^{-/-}$)(**Figure 5A-B**). Consistent with the CRISPRi analysis, we find that all three knockouts can differentiate to CMs (**Supplemental Figure S5A**). We observe that deletion of TBX5 enhancers phenocopies TBX5 gene deletion, with all knockout clones exhibiting reduced RNA expression by qPCR and protein expression by immunocytochemistry (**Figure 5C-E**).

Next, to test if genetic deletion of enhancers contributes to deficient CM specification, we repeated our scRNA-Seq analysis at day 8 of CM differentiation (**Supplemental Figure S5A and Table S3**). Mirroring the CRISPRi results, analysis of all cell populations shows a strong depletion of CM states in perturbed cells (**Figure 5F and Supplemental Figure S5B**). TBX5Enh5$^{-/-}$ cells exhibited the strongest depletion (~9% CMs, p > 2.2e-308, hypergeometric test) relative to WT control cells (~57% CMs), followed by TBX5Enh3$^{-/-}$ cells (~24% CMs, p =

5.2e-263, hypergeometric test), and TBX5Exon$^{-/-}$ cells (~33% CMs, p = 5.9-166, hypergeometric test). Importantly, we observed consistent results over multiple biological replicates.

To examine if enhancer deletion also contributes to deficient CM differentiation, we focused our analysis on a cluster of TNNT2+ cells. Sub-clustering revealed three CM states: FN1+ early CMs, ACTA2+ mid CMs, and NPPA+ late CMs (**Figure 5G**). While cells derived from each genetic background were represented across all 3 states (**Figure 5H and Supplemental Figure S5C**), we observed notable differences. Notably, perturbed cells were on average 10.6-fold less likely to reach the mature late CM state (~27% WT_{Late_CM}, ~5% $Enh3^{-/-}{}_{Late\_CM}$, ~11% $Enh5^{-/-}{}_{Late\_CM}$, ~1% $Exon^{-/-}{}_{Late\_CM}$) and this observation was statistically significant (p_{Enh3} = 1.8e-24, p_{Enh5} = 1.6e-7, p_{Exon} = 5.8e-83) (**Figure 5I**). Next, we repeated our previous analysis to confirm that cells with TBX5 enhancer or exon deletion exhibit elevated expression of mid-CM genes (**Figure 5J**). Importantly, deletion of either TBX5 enhancer or exon 3 resulted in the repression of key genes of cardiac development including the TBX5 target gene NPPA (**Figure 5K, Supplemental Figure S5D, and Table S4**) (Houweling et al., 2005). To confirm this result using an orthogonal assay, we performed RNA fluorescence in situ hybridization coupled to a flow cytometry readout (FlowFISH) (Fulco et al., 2019; Reilly et al., 2021). Consistent with an increase in earlier stage CMs, we find that TBX5 gene and enhancer knockouts have increased RNA and protein expression of early CM markers such as FN1 (**Figure 5L-5N and Supplemental Figure S5E**). Also, consistent with depletion in later stage CMs, we observe that TBX5 gene and enhancer deletions have decreased RNA and protein expression of the late CM marker NPPA (**Figure 5C-5D**).

Finally, since our analyses also generated clones with heterozygous TBX5 enhancer deletion (**Figure 5B**), we performed further analysis of one clone: TBX5Enh5$^{+/-}$ (**Figure 6A-6B).** Confirming that these genetic modifications alter TBX5 expression, we observed that clones with enhancer deletions exhibit significantly decreased RNA expression during CM differentiation (**Figure 6C**). After CM differentiation and scRNA-Seq (**Figure 6D and Supplemental Figure S6A)**, TBX5 Enh5 heterozygous knockouts also exhibited significant depletion of CM states (~24% CMs, p = 5.2e-125, hypergeometric test) relative to WT cells (~45% CMs) (**Figure 6E and Supplemental Figure S6B)**. Sub-clustering of a TNNT2+ cluster revealed four CM states: FN1+ early CMs, ACTA2+ mid CMs, HAND1+ late CMs, and IRX2+ ventricular CMs (**Figure 6F and Supplemental Figure S6C**). Consistently, focused pseudotime analysis of cardiomyocytes also showed significant depletion of Enh5$^{+/-}$ cells in the mature ventricular CM state (~39% WT_{Ven_CM}, ~6% $Enh5^{+/-}{}_{Ven\_CM}$, p = 1.5e-75) (**Figure 6G-6H**). Importantly, heterozygous deletion of TBX5 Enh5 results in a weaker differentiation defect than homozygous deletion of TBX5 Enh3 (which has a weaker phenotype compared to homozygous deletion of TBX5 Enh5) (**Figure 6G-6H**). These observations are consistent with those observed for the TBX5 gene deletions previously published (Kathiriya et al., 2021). Next, we repeated our previous analysis to confirm that cells with TBX5 enhancer knockout exhibit delayed activation of late-CM genes (**Figure 6I**) and delayed repression of mid-CM genes (**Figure 6J**). Our analysis also revealed a depletion of cardiac related genes in perturbed late CM cells compared to controls (**Figure 6K and Table S6**). Cell label transfer onto all previous datasets showed expected clustering consistent deficiencies to achieve later CM states (**Supplemental Figure S6D-S6G**).

In sum, these observations with TBX5 enhancer deletion cells are consistent with our CRISPRi studies, and support the conclusion that loss of TBX5 enhancer function results in deficient transcriptional specification of CMs.

DISCUSSION

This study identifies and functionally characterizes 16 enhancers that are required for normal cardiomyocyte differentiation. Perturbations of these enhancers yield diverse cellular phenotypes ranging from global reduction of mesoderm populations to deficient CM differentiation. These cell specification defects are consistent with the putative role of these enhancers in regulating known cardiac regulators such as TBX5 (Kathiriya et al., 2021). The diversity of cellular responses has several implications. First, our observations highlight the important role of enhancers in orchestrating spatiotemporal gene regulation in development (Plank and Dean, 2014). Second, that enhancer perturbation can lead to such diverse cellular consequences further highlights the potential role of genetic variants in modifying enhancer function and contributing to developmental defects such as CHD (Richter et al., 2020; Smemo et al., 2012). We speculate that focused sequencing of genetic variants at these enhancers will reveal new genetic contributors of CHD. Third, the diversity of cellular responses observed through enhancer perturbation suggests that the cellular phenotypes of CHD could also be very diverse, and that subtle changes in cell fate may lead to complex CHD phenotypes. Indeed, CHD is a diverse developmental disease with multiple causal genes and distinct disease subtypes (van der Linde et al., 2011).

TBX5 presents a potential framework for studies to understand the genetic basis of human developmental disorders by linking human genetic linkage studies (strongest evidence of variant function) to variants of unknown significance (least support). For example, coding variants at TBX5 cause cardiac defects such as Holt-Oram Syndrome (Basson et al., 1997; Bruneau et al., 1999; Holt and Oram, 1960; Li et al., 1997). Consistently, gene knockout studies in human iPSCs have shown that dosage-sensitive impairment of TBX5 alters CM differentiation with CHD-relevant phenotypes (Kathiriya et al., 2021). Even though multiple enhancers control TBX5 expression (Smemo et al., 2012), our studies show that perturbation of TBX5 enhancers exhibit similar cell state phenotypes. Enhancers in close proximity to genes with known roles in CHD represent key targets for future investigation.

Interestingly, our results indicate that knockdown of TNNT2 results in transcriptional phenotypes. While TNNT2 is not known to function as a transcriptional regulator, recent results from similar screens have identified unexpected gene expression phenotypes for genes not typically associated with regulatory function. For example, Replogle et al showed that knockdown of chromosome segregation genes (with unclear roles in transcription) resulted in gene expression phenotypes (Replogle et al., 2022). Similarly, genes with roles in glycolysis, vesicular trafficking, and DNA replication also unexpectedly caused transcriptional changes. These observations make possible the systematic assessment of genotype-phenotype relationships by using the transcriptome as a readout. Thus, TNNT2 knockdown may impact transcriptional states through similarly unexpected effects. One possibility is that, since TNNT2 is a critical component of the sarcomeric apparatus, its loss could initiate a feedback response resulting in delayed CM specification. In support of this possibility, we observe that CRISPRi perturbations of two TNNT2 enhancers and the promoter consistent yield changes in transcriptional and cell state phenotypes (**Figure 2G**, **2I**).

This study represents a proof of concept for future efforts to systematically test the function of enhancers in heterogeneous developmental systems. We adopted a tiered approach to balance the advantages and disadvantages of CRISPR and CRISPRi approaches (Diao et al., 2017; Fulco et al., 2016; Gasperini et al., 2017; Thakore et al., 2015; Zhou et al., 2014). That is, while CRISPRi-based epigenetic silencing can efficiently act across many cells in a population, it offers incomplete inhibition. In contrast, the generation of genetic knockout using CRISPR is

relatively inefficient, but yields clones with complete enhancer deletion. Thus, we started the study with a higher throughput single-cell CRISPRi screens as a filter for potential hits. To ensure robustness, we validated these hits with a smaller scale CRISPRi validation screen. Finally, to ensure consistency with orthogonal perturbation paradigms, we performed clonal enhancer deletion studies. This tiered approach allowed us to balance speed with accuracy. Tiering strategies such as this and others (Klann et al., 2021) will aid future efforts. Importantly, we found that consistent cellular phenotypes can be obtained with both CRISPRi or CRISPR strategies. Expectedly, perturbations of promoters generally yield stronger cellular responses than enhancers. Similarly, genetic knockouts elicit more dramatic changes in cell state than CRISPRi with dCas9-KRAB. Genetic variants likely yield even weaker phenotypes. In this way, we speculate that epigenetic perturbation more closely matches variants than genetic deletion.

Despite the overall success of our screening approach and subsequent validation experiments, we note several potential limitations. First, scRNA-seq provides deep cellular coverage at the expense of sequencing depth per cell, such that detection of lowly expressed genes is challenging. Thus, conclusive determination of sgRNA functionality in individual cells remains problematic. Second, enhancers are known to function in a time-dependent manner, yet sgRNA perturbations were introduced at a fixed time point. While we expect time-dependent perturbations to yield insights on enhancer-mediated gene regulation, one technical challenge is that the temporal delay between perturbation induction and functional repression needs to be resolved and likely improved before application in dynamic developmental systems. Third, CM differentiation in two dimensional culture systems does not adequately recapitulate the complex morphological and inter-cell communication events that occur during human development. Standard cardiac differentiation strategies are very efficient but use harsh metabolic selection to enrich for cardiomyocytes. In our study, we intentionally avoided metabolic selection to preserve non-cell autonomous interactions, since selection may inadvertently mask the phenotypes of genetic perturbations. By eliminating the metabolic selection step during hESC differentiation, we produced heterogeneous cell states including mesodermal (cardiomyocytes and progenitors), ectodermal (neuronal), and endodermal states. This strategy was previously used by Tohyama et al (Tohyama et al., 2013). In support of the relevance of this system, Zic2 is required for early specification of cardiomyocytes. In our system, CRISPRi knockdown of Zic2 results in loss of cardiomyocyte and neuronal specification. These cells with Zic2 sgRNAs are almost entirely diverted to the mesodermal lineage (**Figure S1H**). These results indicate that our biological system captures expected phenotypes and suggest that the results from other perturbations are also potentially relevant to CHD. Future utilization of organoid systems is likely to better mimic the complex morphogenetic changes that occur in vivo.

In summary, we have applied single-cell screening technology to functionally characterize enhancers in a heterogeneous developmental system. We expect future applications of these approaches will help to comprehensively identify enhancers with roles in cell fate specification that could also contribute to developmental defects such as CHD.

ACKNOWLEDGEMENTS

We acknowledge the BioHPC computational infrastructure at UT Southwestern for providing HPC and storage resources that have contributed to the research results reported within this paper. G.C.H is supported by CPRIT (RP190451), NIH (DP2GM128203, UM1HG011996, 1R35GM145235), the Burroughs Wellcome Fund (1019804), the Welch Foundation (I-2103-20220331), and the Green Center for Reproductive Biology. N.V.M. was supported by

the NIH (HL136604, HL151650, and UM1HG011996), the Burroughs Wellcome Fund (1009838), and the Department of Defense (PR172060).

COMPETING INTERESTS

The authors declare no competing interests.

STAR METHODS

KEY RESOURCES TABLE

Reagent	Source	Identifier
Chemicals, Peptides, and Recombinant Proteins		
Puromycin	Cayman Chemical	Cat#13884
Blasticidin	RPI	Cat#3513-03-9
Thiazovivin	Sigma-Aldrich	Cat#SML1045
TrypLE Select	ThermoFisher	Cat#12563
CHIR99021	Tocris	Cat#4423
Wnt-C59	Cayman	Cat#16644
Accutase	Sigma-Aldrich	Cat#SCR005
Insulin	Gibco	Cat#12585014
B-27	ThermoFisher	Cat#17504044
Molecular Probes Fura-2	ThermoFisher	Cat#F1221
Pluronic F-127	ThermoFisher	Cat#P6867
FN1 Polyclonal Antibody	ThermoFisher	Cat#PA5-29578
Anti-rabbit IgG	Cell Signaling Technology	CST #7074
Critical Commercial Assays		
KAPA HiFi HS	KAPA	Cat#KK2502
PrimeFlow RNA Assay Kit	ThermoFisher	Cat#88-18005-210
NEBNext High-Fidelity	New England Biolabs	Cat#M0541L
Gibson Assembly Master Mix	New England Biolabs	Cat#E2611L
mTeSR Plus	Stemcell Technologies	Cat#100-0276
Matrigel	Corning	Cat#354277
P3 Primary Cell 4D-Nucleofector X Kit	Lonza	Cat#V4XP-3024

10X genomics Chromium Single Cell 3′ Kit V3.1	10X Genomics	Cat#PN-1000147
10X CellPlex	10X Genomics	Cat#PN-1000261
10X Target Hybridization Kit	10X Genomics	Cat#PN-1000248
RPMI 1640	ThermoFisher	Cat#11875093
KnockOut Serum	ThermoFisher	Cat#10828028
HHBSS	Corning	Cat#21-023-CM
Bacterial and Viral Strains		
Endura ElectroCompetent Cells	Lucigen	Cat#60242-2
Stellar Competent Cells	Clontech	Cat#636766
Deposited Data		
Single-cell RNA-seq Data	This paper	GEO: GSE190475
Experimental Models: Cell Lines		
293T cells	ATCC	ATCC CRL-3216
H9 cells	WiCell	WA09
Recombinant DNA		
Plasmid: pMD2.G	Addgene	Addgene 12259
Plasmid: psPAX2	Addgene	Addgene 12260
Plasmid: lenti-dCas9-KRAB-Blast	Addgene	Addgene 89567
Plasmid: CROPseq-Guide-puro	Addgene	Addgene 86708
Sequence-Based Reagents		
sgRNA Oligos	Table S1	N/A
qPCR primers	Table S2	N/A
Software and Algorithms		
Star	Dobin et al., 2013	https://github.com/alexdobin/STAR

Picard	Broad Institute	https://broadinstitute.github.io/picard/
FlowCal	Castillo-Hair et al, 2016	https://taborlab.github.io/FlowCal/index.html
FeatureCounts	Liao et al., 2014	http://bioinf.wehi.edu.au/featureCounts/
10x Genomics Cellranger	10x Genomics	https://support.10xgenomics.com/single-cell-gene-expression/software/pipelines/latest/what-is-cell-ranger
Scanpy	Wolf et al., 2018	https://scanpy.readthedocs.io/en/stable/
IGV	Broad Institute	N/A
Other		
Illumina NextSeq 500 instrument	Illumina	N/A
Illumina NextSeq 2000 instrument	Illumina	N/A
Illumina NovaSeq 6000 instrument	Illumina	N/A
Agilent 2200 TapeStation instrument	Agilent	N/A
Qubit Fluorometric Quantitation instrument	ThermoFisher	N/A
EVOS FL Auto Imaging System	ThermoFisher	N/A

Sample Generation

Generation of PiggyBac dCas9-KRAB Plasmid

The NheI/SalI dCas9-KRAB fragment from Lenti-dCas9-KRAB-blast (Addgene ID: 89567) was ligated into PiggyBac vector 5'-PTK-3' (Cadiñanos and Bradley, 2007) replacing the NheI/SalI insert. A bovine growth hormone polyadenylation signal was PCR amplified (Kapa HiFi DNA polymerase) (5'-GCC TCC CCG CAT CGA TAC CGC TGT GCC TTC TAG TTG CCA G, 3'-GTA ACA AAA CTT TTA ACT AGC CAT AGA GCC CAC CGC ATC C) and assembled (NEB HiFi Assembly) replacing the remaining SalI/SpeI fragment. A 647 bp ubiquitous chromatin opening

element (UCOE), derived from the human HNRPA2B1-CBX3 locus was PCR amplified (5'-TAT AGA TAT CAA CTA GAA TGG GGA GGT GGT CCC TGC AG, 3'-AAC TTT ATC CAT CTT TGC AGG GCC CTC CGC GCC TAC AG) and assembled into the NheI site.

Target Selection

14 enhancers were selected using publicly available ATAC-seq and H3K27ac ChIP-seq datasets collected at various time points throughout CM differentiation. ATAC-seq peaks across all timepoints were merged and extended to a total size of 500bp. We then applied FeatureCounts for H3K27ac ChIP-seq signal at these 500bp ATAC-seq boundaries. H3K27ac counts were normalized to RPKM then to input followed by $\log_2$ transformation. We selected for ATAC-seq regions in which the max ChIP enrichment across all timepoints was greater than $\log_2(1.5)$, identifying 43,536 enhancers across CM differentiation. We then selected enhancers which were within 1kb of a CHD-associated variant which left 2,300 CHD-associated enhancers. Using gene ontology, we identified enhancers which were within 100kb of a heart development associated gene. After manually filtering for genes based on prior literature, we were left with 14 enhancers. We also included the 18 nearby promoters for heart development genes. Our library also consisted of 6 TBX5 enhancers, 3 we identified in house using the same criteria above with the expectation of CHD variant overlap, and 3 from literature (Smemo et al., 2012). From a MPRA study, we also selected 5 enhancers in which CHD-associated variants have been shown to perturb activity (Richter et al., 2020).

Generation of sgRNA Library

We used CROPseq-Guide-Puro plasmid for sgRNA expression (Addgene ID: 86708). For large screen sgRNA library construction, a single-strand sgRNA oligo library containing 397 sgRNAs (**TableS1**) was synthesized by IDT. The library was amplified by NEBNext High-Fidelity 2X PCR master mix (New England Biolabs) to make it double-stranded and then was inserted into the BsmBI digested CROPseq-Guide-Puro plasmid through Gibson Assembly (New England Biolabs). The circulized product was purified and electroporated into Endura ElectroCompetent cells (Lucigen) following the manufacturer's protocol. The cells were then cultured in LB medium with 100µg/ml Ampicillin at 30°C overnight and the plasmid extracted using the ZymoPURE plasmid maxiprep kit (Zymo Research). We amplified the spacer sequences of the sgRNA library and verified the complexity of the library by Illumina sequencing. See our previous publication for a full protocol including primer sequences (Xie et al., 2019). Our focused screen consisted of 49 sgRNA which were packaged using a golden gate strategy previously published. In brief, single-strand sgRNA oligos were ordered from IDT and annealed using T4 ligase. Annealed oligos for sgRNA targeting the same region were then pooled for a golden gate reaction using BsmBI and T7 ligase to insert the sgRNA into the CROPseq backbone. Individual sgRNA were packaged in a similar approach.

Cell Line

H9 ESCs were maintained feeder-free in mTeSR Plus (Stemcell Tech. 100-0276) according to suggested manufacturer's instructions on Matrigel (Corning 354277) coated plates, passaged every 3-4 days with DPBS/0.5 mM EDTA and plated in 2 uM thiazovivin (Sigma SML1045) supplemented mTeSR Plus overnight.

Generation of dCas9-KRAB-hESC Line

H9 ESCs were washed with DPBS and dissociated to single cells with TrypLE Select. Transfection of $1x10^6$ cells with 5 ug PiggyBac transposon plasmid and 1 ug HA-mPB (Cadiñanos and Bradley, 2007) transposase plasmid in 100 ul was performed using P3 Primary Cell 4D-Nucleofector X Kit (V4XP-3024) with program CB-150 according to suggested manufacturer's instructions. At confluency cells were passaged and maintained in the presence

of 5 ug/ml blasticidin S until emerging colonies were ~1 mm in diameter. Individual colonies were isolated, expanded and tested for stable expression.

CM Differentiation

At 80-90% confluency, media was replaced with 3 uM CHIR99021 supplemented CDM3 (RPMI 1640; 0.5 mg/ml human albumin, ScienCell OsrHSA; 211 ug/ml L-ascorbic acid 2-phosphate) for 48 hours followed by 2 uM Wnt-C59 supplemented CDM3 for 48 hours with subsequent media changes every 2 days with CDM3 alone. On day 8 post-differentiation, samples were washed with DPBS and dissociated to single cells with Accutase and resuspended in CDM3.

Virus Packaging

Lentiviral plasmid was packaged as previously described (Xie et al., 2019). Briefly, the lentivirus packaging plasmids PMD2.G and psPAX2 (Addgene ID: 12259 and 12260) were co-transfected with the carrier plasmid to HEK293T cells with linear polyethylenimine (PEI, Polysciences). Supernatant was collected 72 h after transfection and filtered with a 0.45μm filter. The virus was further purified by using Lenti-X lentivirus concentrator (Clontech).

sgRNA Transduction

Single cell dissociated H9 ESCs ($1x10^6$ cells) were incubated in 2 ml medium supplemented with thiazovivin and lentiviral supernatant (MOI ~0.3) in a single well of an ultra-low attachment plate (Corning 3471) for 3 hours, diluted in 2 ml medium and then plated onto three wells of a Matrigel coated 6-well plate. At 72 hours post-transduction cells were fed with 5 ug/ml blasticidin S and 1 ug/ml puromycin supplemented medium for 7 days.

Knockout Line Generation

Transfection of 10 ug Cas9/sgRNA plasmids (left and right flanking at 1:1) was performed as described in stable line generation. At 48 hours post transfection, single GFP positive cells were sorted, expanded, and isolated for knock-out validation. For validation, genomic DNA was extracted with QuickExtract (Lucigen) and PCR was performed to verify deleted regions.

Immunocytochemistry

Cells were differentiated or passaged on Matrigel coated #1.5 12 mm cover glass. Cells were washed with DPBS, fixed with 4% PFA in DPBS for 20 min. at room temperature and washed with DPBS. Samples were blocked for 1 hour with PBS supplemented with 5% normal donkey serum and 0.3% Triton X-100. Primary antibodies in PBS supplemented with 1% BSA and 0.3% Triton X-100 were incubated overnight at 4°C. After 3x5 min. washes with PBS, secondary antibodies at 1:400 were incubated at room temperature for 2 hours, washed, mounted with Prolong Glass (Invitrogen P36981) and imaged with an EVOS FL Auto Imaging System (ThermoFisher).

Western Blotting

Whole-cell protein lysate was collected using RIPA buffer in the presence of protease inhibitors and PMSF. After protein concentration was determined, the lysate was denatured in 2X Laemmli Sample Buffer, separated by electrophoresis, and transferred to Nitrocellulose membrane. Membranes were blocked with 5% non-fat dry milk in TRIS buffer containing 0.1% Tween-20 (TBST) for 1 hour followed by incubation with primary antibody overnight at 4°C. The membranes were then washed with TBST followed by application of appropriate HRP-conjugated secondary antibody for 1 hour at room temperature. After washing with TBST, membranes were incubated with Pierce SuperSignal West Femto and images with a BioRad ChemiDoc Imager.

FlowFISH

TBX5 exon 3, enhancer 3, enhancer 5, and WT H9 hESC were differentiated into CMs over 8 days followed by PrimeFlow following the commercial protocol. Each sample was multiplexed for FN1 (Alexa 647) and RPL13A (Alexa 488) probes followed by flow cytometry. Data was analyzed using the FlowCal python package (Castillo-Hair et al., 2016). Gating was performed using the density function along the forward scatter and side scatter axes. Briefly, the function takes in the percentage of events to retain as an input. Then, the plot is divided into grids and events in those grids are counted. A histogram is plotted, and the curve is smoothened using Gaussian blur. For this analysis, 45% of events were retained and further analysis was done using gated data. To normalize FN1, FN1 probe intensity was divided with RPL13A probe intensity at a single cell level for all the samples.

Single-cell RNA-seq

For the focus screen, dissociated CMs were resuspended in 0.08% BSA in PBS and passed through a 70 micron filter before diluting to 1,000 cells/uL. 2 10X lanes were run at an expected recovery of 10,000 cells. For the initial screen, dissociated CMs were divided into 10 samples consisting of 5*10^5 cells and each sample stained with one of 10 cell hashing bodies. Cells were processed as described in cell hashing publication (Stoeckius et al., 2018). After processing, cells were resuspended in 0.04% BSA in PBS and diluted to 4,800 cells/uL. 8 10X lanes were run at expected recovery of 45,000 cells. For sequencing exp (**Fig 5 and Fig 6**), divided knockout and control dissociated CMs into 12 samples of 1*10^6 cells and stained each using a unique CellPlex oligo. Samples were processed as in 10X Genomics Chromium 3' V3.1 with Cell Multiplexing kit and pooled together evenly for a final concentration of 1,500 cells/uL in 0.04% BSA in PBS. For sequencing exp (**Fig 5**), 2 10X lanes were run at an expected recovery of 30,000 cells. Single-cell RNA-seq libraries were prepared using 10X Genomics Chromium 3′ V3.1 kit, following the standard protocol. For sequencing exp (**Fig 6**), 2 10X lanes were run at an expected recovery of 60,000 cells. Single-cell RNA-seq libraries were prepared using 10X Genomics Chromium 3′ V3.1 HT kit, following the standard protocol. To construct the sgRNA enrichment libraries, 50 ng of cDNA product was used to perform an enrichment PCR using SI-PCR primer and sgRNA enrichment primers. The PCR product was purified using a 1.6X SPRI beads cleanup followed by a final index PCR using SI-PCR primer and Nextera primers. A final 1.6x SPRI beads cleanup was then performed with a final expected library size of 500bp. To construct cell hashing libraries, 20uL of supernatant fraction cDNA was used for hashtag amplification PCR using SI-PCR primer and Nextera Hashtag primers. For a more detailed protocol see cell hashing publication (Stoeckius et al., 2018). To construct CellPlex libraries, followed 10X Genomics Chromium 3' V3.1 and V3.1 HT kit with Cell Multiplexing. To construct targeted gene expression libraries for initial screen, amplified transcriptome libraries following the 10X Genomics library re-amplification protocol. Following re-amplification, libraries were pooled and targeted gene expression libraries constructed as in the 10X Genomics protocol.List of probes and primers used in (**TableS1**).

Sequencing

Libraries were sequenced through a combination of Illumina NovaseqS4, NextSeq 500/550, and NextSeq 2000. We used paired-end sequencing using the following settings: R1-151bp R2-151bp idx1-10bp idx2-10bp on Novaseq; R1-28bp R2-54bp idx1-10bp and R1-28bp R2-56bp idx1-8bp on NextSeq 500/550; and R1-28bp R2-90bp idx1-10bp idx2-10bp on NextSeq 2000. All sequencing data is available on GEO: GSE190475

Data Processing

Mapping

For the initial screen and focus screens, scRNA-seq libraries were demultiplexed and mapped to the human reference genome (hg38) using the Cellranger software (ver 3.1.0, 10X Genomics). Focus screen experiments were mapped using Cellranger count with the following flags; --expect-cells = 10000, and --chemistry = SC3Pv3. Initial screen experiments were mapped using Cellranger count with the following flags; --feature-ref (cell hashing library), --expect-cells = 45000, and --chemistry = SC3Pv3. Cell hashing antibody assignments were included as a feature barcode. scRNA-seq mapped libraries for each experiment were combined using Cellranger aggr and normalized for sequencing depth using the flag --normalization = mapped. Sequencing exp (**Fig 5**) was mapped to the human reference genome (hg38) using the Cellranger software (ver 6.0.0, 10X Genomics) with Cellranger multi using the following parameters; --expect-cells = 30000 and --chemistry SC3Pv3. Sequencing exp (**Fig 6**) was mapped to the human reference genome (hg38) using Cellranger software (ver 6.1.2, 10X Genomics) with Cellranger multi using the following parameters: --expect-cells = 60000 and --chemistry SC3Pv3HT. Cellplex oligo assignments were included as a feature barcode. Cellplex demultiplexed libraries were aggregated using Cellranger aggr and normalized for sequencing depth using the flag --normalization = mapped. sgRNA libraries were mapped using FBA (Duan and Hon, 2021). FBA extract was run using a mismatch of 1 with --r1_coords 0,16 and --r2_coords 19,38. Following sgRNA sequence extraction, FBA count was run. Initial screen targeted gene expression libraries were mapped to the human reference genome (hg38) using Cellranger (ver 6.1.2, 10X Genomics) count with the following flags; --expect-cells = 45000, and --chemistry = SC3Pv3. Initial screen targeted gene expression libraries were aggregated using Cellranger aggr and normalized for sequencing depth using the flag --normalization = mapped.

Single-Cell Processing

We assigned sgRNA to cells using the saturation curve method described in Drop-seq (Macosko et al., 2015). For a given sgRNA, we calculated the cumulative distribution of the UMIs from all cells. By identifying the inflection point of the curve, we adjusted the UMIs from cells after the inflection point to be zero. The sgRNAs with the adjusted UMI count greater than 0 are considered as true sgRNAs in this cell. To process cell hashing antibodies, we applied a saturation curve in a similar method as with the sgRNA processing.

We filtered for only singlets using Scrublet in the focused screen. In our initial screen, cells in which only one antibody barcody was detected were retained. Cells with higher than 20% mitochondrial content were removed, as well as genes with fewer than 1 counts. The count matrix was natural log transformed and saved as a separate layer for differential gene expression calling before scaling counts to unit variance and zero mean. An extra filter was applied to the initial screen in which cells where we could not detect an sgRNA were removed. Post filtering we were left with 80,147 cells in the initial screen. Clustering was performed through Scanpy implementations (Wolf et al., 2018). Briefly, PCA was performed followed by neighborhood calculation using default parameters. We then clustered cells using the Louvain algorithm at 0.2 resolution for initial and focus screens, 0.15 resolution for sequencing exp (**Fig 5**), and 0.1 resolution for sequencing exp (**Fig 6**). PAGA was performed to map cluster connectivity and served as the embedding for UMAP visualization, which was applied with default settings. Clusters which held fewer than 1% of all cells were removed. This resulted in

22,214 single cells in the focus screen, 31,367 cells in sequencing exp (**Fig 5**), and 24,571 in sequencing exp (**Fig 6**).

We applied the rank_gene_groups function of scanpy to identify cluster defining genes using the Wilcoxon rank-sum method. In our initial screen, we identified the following populations: two neuronal (+SOX2), cardiomyocytes (+TNNT2), mesoderm (+FN1), epithelial (+EPCAM), cardiac fibroblast (+COL3A1), and endoderm (+TTR). In our focus screen, we grouped similar clusters together and defined the following cell types: neuronal (+SOX2), cardiomyocytes (+TNNT2), endoderm (+TTR), and endothelial (+PECAM1). Similar clusters were observed in sequencing exp (**Fig 5 and Fig 6**). For all experiments, we identified the enriched genes defining each Louvain cluster by applying the Scanpy rank_gene_groups function using the Wilcoxon rank-sums method.

Single-Cell Trajectory Clustering

To identify CM trajectory, clusters were filtered to retain cell populations relevant to cardiac differentiation. We isolated Louvain clusters corresponding to CMs in the focus screen and initial screen. The mesoderm cluster was included in the initial screen due to its involvement in CM differentiation. We then clustered these cells using PCA and PHATE with k=10/a=20 for the focus screen, k=30/a=100 in the initial screen, k=10/a=100 in sequencing exp (**Fig 5**), and k=10/a=50 in sequencing experiment (**Fig 6**). Neighborhood calculation and Louvain clustering at resolution 0.83 for the focus screen, 0.3 for the initial screen, 0.6 in sequencing experiment (**Fig 5**), and 0.7 in sequencing experiment (**Fig 6**) were applied to generate new clusters. We selected the clusters corresponding to CM and smooth muscle markers resulting in 1,832 focus screen, 17,716 initial screen, 4717 sequencing experiment (**Fig 5**),and 4,871 sequencing experiment (**Fig 6**) CM cells. The above clustering process was then repeated using k=10/a=20 for the focus screen, k=60/a=100 for the initial screen, k=10/a=100 in sequencing exp (**Fig 5**), and k=20/a=100 for sequencing experiment (**Fig 6**). We applied the Louvain algorithm to the initial screen, focus screen, and sequencing experiment (**Fig 5**) at resolution 0.3. For sequencing exp (**Fig 6**), an initial broad Louvain clustering was identified using resolution 1.2. This was used to identify the root mesoderm-like cluster for pseudotime calling. Following, a final resolution of 0.4 was applied. Louvain clustering identified SOX4+ progenitor, FN1+ early CMs, ACTA2+ mid CMs, and NPPA+ atrial-like late CMs in our initial screen. Our focus screen identified 3 clusters comprising progenitor, mid and late CMs. Sequencing exp (**Fig 5**) consisted of 3 clusters comprising early, mid, and late CMs. Sequencing exp (**Fig 6**) consisted of 4 clusters comprising early, mid, late and IRX2+ ventricular CMs. To verify the integrity of the PHATE projected trajectory, we ran diffusion pseudotime as implemented in Scanpy dpt. Clusters reminiscent of mesoderm-like cells were selected as the roots for all projections.

We applied the ingest module of Scanpy to transfer CM cluster labels across datasets as validation. We assigned the initial screen as reference and transferred labels onto focus screen CMs. Sequencing exp (**Fig 6**) was also assigned as reference and labels transferred onto other CM datasets. Perturbation CM distribution analysis was repeated across all label transfer re-assignments.

sgRNA Filtering

We designed multiple sgRNA for each candidate enhancer and promoter to account for potential off-targets. To identify sgRNA with off-target effects or that were non-functional, we applied a filtration approach using the identified CM trajectory in the large experiment. First we filtered our 5 non-target sgRNA to create a background. This was done by using a hypergeometric test for each CM cluster to compare the distribution of cells with each individual NT to the background of cells with any NT. We performed the hypergeometric test 5 times, in each iteration removing

one of the NT. Through this we identified one NT which, if included, produced bias in the background distribution. After removing this NT, we were left with 4 similarly distributed controls which served to define our control cells for downstream analysis.

Second, for each target, we filtered to remove sgRNA that deviated in distribution to the majority. For each possible combination of sgRNA cells for each target, we performed a hypergeometric test for each CM cluster comparing the distribution of these sgRNA cells to the filtered NT cells background. For each of 4 CM clusters, we had two lists of p-values, one for depletion of sgRNA cells and one for enrichment. This resulted in a total of 8 p-value lists. We then ordered each resulting p-value list for all sgRNA combinations in descending order of significance. A cutoff was drawn corresponding to the number of times each sgRNA is found in a given combination. We then asked whether any given sgRNA for this target was found at a significant rate to the left of this cutoff by using a hypergeometric test. If an sgRNA was found to be uniquely biased in this direction, it was removed. This was repeated for all 8 p-value lists. If more than half of the sgRNA for a given target would be removed by this approach, all sgRNA were kept. This was repeated for sgRNA targeting every enhancer and promoter. All analysis, including validation experiment, used this filtered sgRNA set.

Quantification and Statistical Analysis

Bulk validation of CM Trajectory

Previously published RNA-seq data from a hESC to CM differentiation time course was mapped to the hg38 reference genome by STAR. For each sample, counts were normalized to RPKM. Replicate counts for each sample were then averaged together. We identified the top 100 uniquely enriched genes for each of our CM subpopulations in the initial screen from the Scanpy rank_gene_groups function using the Wilcoxon rank-sums method. For each enriched cluster gene set, fold change over day 0 was calculated for every time point. The fold changes of each gene from a gene set were then averaged by time point.

Comparison of sgRNA Distribution

Clustering bias was performed in a similar manner for every dataset. We compared the distribution of sgRNA for a given target to NT sgRNA across cell clusters using a hypergeometric test. Depletion of sgRNA was calculated using the hypergeometric cumulative distribution function and enrichment by using the survival function.

To compare the distribution of sgRNA across CM trajectory pseudotimes, we applied a Mann-Whitney U test which identified whether the median pseudotime for a given target was significantly shifted from NT control.

Differential Expression of Cell Type Defining Gene Sets

We applied a Wilcoxon Rank-Sum test using Scanpy integration to compare gene expression of late CMs and mid CMs from our focused screen. This approach identified 18 genes significantly enriched in mid CMs and 80 genes enriched in late CMs. To assess the expression of these gene sets in NT control vs sgTBX5 ENH cells within the late CM population, we calculated the average expression of this gene set within all our sgTBX5 ENH cells in late CM. As significantly more NT cells (558) achieved a late CM fate in comparison to sgTBX5 ENH cells (122), we obtained a control expression distribution by sampling 122 NT cells through 1000 iterations and recording the average expression of genes sets each time. We applied a z-test comparing

perturbed to control expression and converted to p-value using scipy.stats.norm.cdf for enrichment and scipy.stats.norm.sf for depletion of gene set expression in perturbed cells. The same z-test methodology was applied to our knockout screen in late CMs comparing focused screen differential gene sets between knockout and WT cells.

Differential Expression

Differential expression of individual genes was calculated by applying a Mann-Whitney U test through scipy.stats.mannwhitneyu to the expression distribution of a given gene in perturbed to NT control cells.

DATA AND CODE AVAILABILITY

The sequencing data generated in this study have been deposited to the Gene Expression Omnibus (GEO) under the accession (GSE190475, reviewer token: obmhkeayzripviv). We have deposited Jupyter notebooks to Github (https://github.com/darmen04/Repression-of-CHD-associated-enhancers-delays-human-cardiomyocyte-lineage-commitment).

FIGURE LEGENDS

Figure 1: Single-cell screens of CHD-associated enhancers during cardiomyocyte differentiation.

A. Genome browser snapshot emphasizing features of a targeted enhancer about 15kb upstream of the RBM20 gene. Yellow highlights enhancer region.
B. H3K27ac and open chromatin (ATAC-Seq) enrichment for targeted enhancers across multiple timepoints of CM differentiation (Liu et al., 2017; Tompkins et al., 2016; Zhang et al., 2019).
C. Expression of putative target genes across multiple stages of CM differentiation. Expression defined as fold change over the day 0 expression of a target gene (Tompkins et al., 2016).
D. Schematic of single-cell CRISPRi screen. H9-dCas9-KRAB cells are infected with a lentiviral sgRNA library and differentiated over 8 days into CMs followed by scRNA-seq. Individual cells are linked to sgRNA perturbations and changes in transcriptional cell state.
E. UMAP visualization of H9-derived cells after 8 days of differentiation. 7 Louvain clusters indicated.
F. Expression of the top 100 cluster defining genes for each Louvain cluster cell type.
G. MALAT1 expression in control (non-targeting) and sgMALAT1 cells (* $p < 0.05$ by Mann-Whitney U).
H. Distribution of cells receiving sgNT, sgTBX5 PROM1, sgTBX5 ENH6 that differentiate into CM and mesoderm states (* $p < 0.05$ and ** $p < 0.001$ by hypergeometric test).

Figure 2: CRISPRi of CHD-associated enhancers delays cardiomyocyte differentiation.

A. PHATE visualization of CM cells with 4 Louvain clusters.
B. Feature plot of pseudotime ranking of cells across PHATE trajectory.
C. Feature plot of TNNT2 expression.
D. We defined the top 100 genes for each of the 4 CM subtypes. Shown is the expression of these gene sets in bulk RNA-Seq experiments of CM differentiation (Tompkins et al., 2016). Expression defined as fold change over day 0.
E. Enrichment (right) and depletion (left) of cells with distinct perturbations across CM sub-populations (p-values: hypergeometric test). Top: Targeted promoters; middle: targeted enhancers; bottom: non-targeting sgRNAs.
F. Genome browser tracks of chromatin and sequence conservation at two putative TNNT2 enhancers (ENH2 and ENH3). Yellow region denotes enhancer boundaries.
G. Distribution of states for cells receiving sgRNAs targeting TNNT2 promoter and enhancers (* $p < 0.05$ by hypergeometric test).
H. Distribution of pseudotime rank for cells receiving sgRNAs targeting TNNT2 promoter and enhancers (* $p < 0.05$ by Mann-Whitney U).
I. Differentially expressed genes in CM cells receiving sgRNAs targeting TNNT2 promoter or enhancers. In this Manhattan plot, the horizontal axis indicates genomic coordinates, with the dotted line indicating the targeted TNNT2 promoter. The vertical axis indicates differential expression (p-value), with positive values representing increased expression and negative values representing decreased expression.
J. Genome browser track of fetal human heart H3K27ac for CHD ENH5. Yellow region denotes enhancer boundaries.
K. Distribution of states for cells receiving sgRNAs targeting CHD ENH5 (* $p < 0.05$ by hypergeometric test).
L. Distribution of pseudotime rank for cells receiving sgRNAs targeting CHD ENH5 (* $p < 0.05$ by Mann-Whitney U).

M. Distribution of states for cells receiving sgRNAs targeting TBX5 promoters and enhancers (* $p < 0.05$ by hypergeometric test).
N. Distribution of pseudotime rank for cells receiving sgRNAs targeting TBX5 promoter and enhancers (* $p < 0.05$ by Mann-Whitney U).
O. Differentially expressed genes in CM cells receiving sgRNAs targeting a TBX5 enhancer (as described in 2I).

Figure 3: A focused validation screen demonstrates that TBX5 enhancers modulate CM cell fate.

A. (Top) Schematic of validation CRISPRi screen. H9-dCas9-KRAB cells are infected with lentiviral sgRNA library targeting TBX5 enhancers and differentiated over 8 days into CMs followed by scRNA-seq. (Bottom) Genome browser tracks of chromatin status and sequence conservation for TBX5 enhancers. Yellow regions denote enhancers.
B. UMAP visualization of H9-derived cells after 8 days of differentiation. 4 Louvain clusters indicated.
C. Expression of the top 100 cluster-defining genes for each Louvain cluster.
D. Feature plots of cells receiving sgRNAs targeting TBX5 enhancers (red) or non-targeting (NT) control (gray).
E. Distribution of cells receiving sgNT and sgTBX5 enhancers that differentiate into CMs (* $p < 0.05$ by hypergeometric test).
F. Expression of ACTA2 (left) and NPPA (right) in sgTBX5 enhancer and control sgNT CMs (* $p < 0.05$ by Mann-Whitney U).

Figure 4: TBX5 enhancer repression alters CM molecular signatures.

A. PHATE visualization of CMs in the focused screen with 3 Louvain clusters.
B. Feature plot of pseudotime ranking of cells across PHATE trajectory.
C. Feature plot of NPPA expression.
D. Single-cell expression of TNNT2 (top) and NPPA (bottom) across pseudotime ordered CMs.
E. Feature plots of cells receiving sgRNAs targeting TBX5 enhancers or non-targeting NT control.
F. Distribution of states for cells receiving sgRNAs targeting TBX5 enhancers or non-targeting NT control (* $p < 0.05$ by hypergeometric test).
G. Distribution of pseudotime rank for cells receiving sgRNAs targeting TBX5 enhancers and NCs (* $p < 0.05$ by Mann-Whitney U).
H. (top) We defined late CM genes as those more expressed in late CM cells. Shown is the average expression of late CM genes in cells across pseudotime. Cells receiving sgRNAs targeting TBX5 enhancers (red) or non-targeting NT control (gray). (bottom) Boxplots of CM subpopulation pseudotime ranks across pseudotime.
I. Average expression of late CM genes across cells receiving sgRNAs targeting TBX5 enhancers (red) and 1000 random samplings of non-targeting control (sgNT) late CM cells (gray) (* $p < 0.05$ by Z-test).
J. (top) For late CM genes, shown is the relative expression in cells receiving sgRNAs targeting TBX5 enhancers compared with non-targeting NT control, across pseudotime. (bottom) Boxplots of CM subpopulation pseudotime ranks across pseudotime.
K. NPPA expression in cells receiving sgRNAs targeting TBX5 enhancers and NC.
L. (top) We defined mid CM genes as those more expressed in mid CM cells. Shown is the average expression of mid CM genes in cells across pseudotime. Cells receiving sgRNAs targeting TBX5 enhancers (red) or non-targeting NT control (gray). (bottom) Boxplots of CM subpopulation pseudotime ranks across pseudotime.

M. Averaged expression of mid CM genes across cells receiving sgRNAs targeting TBX5 enhancers (red) and 1000 random samplings of non-targeting control (sgNT) late CM cells (gray) (* p <0.05 by Z-test).
N. (top) For mid CM genes, shown is the relative expression in cells receiving sgRNAs targeting TBX5 enhancers compared with non-targeting NT control, across pseudotime. (bottom) Boxplots of CM subpopulation pseudotime ranks across pseudotime.
O. HAS2 expression in cells receiving sgRNAs targeting TBX5 enhancers and non-targeting NT control.

Figure 5: TBX5 enhancer knockouts recapitulate CRISPRi phenotypes.

A. (top) TBX5 enhancer knockout strategy. (bottom) Genome browser snapshots of chromatin status and sequence conservation. Dotted lines denote sgRNA target sites.
B. Genotyping PCR to verify TBX5 knockouts of exon 3 (top), enhancer 3 (middle), and enhancer 5 (bottom). Red asterisk indicates clones used in downstream analysis.
C. NPPA transcript expression in exon and enhancer knockout cells after 8 days of CM differentiation. qPCR quantification normalized to reference gene (RPLP0) and then compared with WT cells.
D. ICC for TBX5 (left) and NPPA (right) in WT and TBX5 exon 3, enhancer 3, and enhancer 5 knockout cells.
E. Quantification of TBX5 ICC (mean intensity) across TBX5 genotyping (* p < 0.05 by Mann-Whitney U).
F. Distribution of WT, TBX5 enhancer KO, or exon KO cells that differentiate into CMs relative to endoderm population (* p < 0.05 by hypergeometric test).
G. (top left) PHATE visualization of CMs with 3 Louvain clusters. (other quadrants) Feature plots of FN1, ACTA2, and NPPA expression.
H. (top left) Feature plot of pseudotime ranking of CM cells across PHATE trajectory. (other quadrants) Distribution of TBX5 exon KO and enhancer KO cells across CM trajectory. WT: gray.
I. Distribution of WT, TBX5 exon KO, and enhancer KO cells across 3 CM subpopulations (* p <0.05 by hypergeometric test).
J. Averaged expression of mid CM genes across TBX5 exon and enhancer KO cells (red) and 1000 random samplings of WT mid CM cells (gray) (* p <0.05 by Z-test).
K. Differentially expressed genes in enhancer 3 KO cells in CM states. Please see description of Manhattan plot in Figure 2I.
L. FN1 transcript expression in exon and enhancer knockout cells after 8 days of CM differentiation. qPCR quantification normalized to reference gene (RPLP0) and then compared with WT cells.
M. (left) Overview of FlowFISH experiment. (right) Flow cytometry of FN1 RNA FISH intensity normalized by control RPL13A intensity in TBX5 WT and KO lines (* p < 0.05 by Mann-Whitney U).
N. (top) FN1 and ACTB (bottom) protein expression in WT, TBX5 exon and enhancer KO cells after 8 days of CM differentiation.

Figure 6: Heterozygous TBX5 enhancer 5 knockout displays reduced phenotypes.

A. TBX5 enhancer 5 heterozygous knockout strategy.
B. (top) Position of primers used to validate TBX5 enhancer 5 heterozygous clone. Red: KO enhancer-spanning primers; blue: left junction primers; orange: enhancer internal

primers; and yellow: right junction primers. (bottom) Genotyping PCR to verify TBX5 enhancer 5 heterozygous deletion. Like the WT, the heterozygous clone retains left, internal, and right fragments, consistent with retaining a copy of enhancer 5. Unlike the WT, the heterozygous clone yields a small fragment when amplified with the KO enhancer-spanning primers. PCR conditions were not optimized for amplification of the WT large 3-kb+ fragment. WT: wild-type; HET: TBX5 enhancer 5 heterozygous clone; B: blank.

C. TBX5 transcript expression in enhancer knockout cells after 8 days of CM differentiation. qPCR quantification normalized to reference gene (RPLP0) and then compared with control cells.
D. (left) UMAP visualization of H9-derived cells after 8 days of differentiation. 4 Louvain clusters indicated. (right) Feature plot of TNNT2 expression.
E. Distribution of WT and TBX5 Enhancer KO cells after differentiation (* p <0.05 by hypergeometric test).
F. (top left) PHATE visualization of CM trajectory cells with 4 distinct Louvain clusters. (other quadrants) Feature plot of FN1, ACTA2, and IRX2 expression.
G. Distribution of TBX5 Enhancer KO cells across CM trajectory. WT: gray.
H. Cell distribution of TBX5 Enhancer KO cells across 4 CM subpopulations. (* p <0.05 by hypergeometric test).
I. Averaged expression of late CM genes across TBX5 Enhancer KO cells (red) and 1000 random samplings of WT late CM cells (gray) (* p <0.05 by Z-test).
J. Averaged expression of mid CM genes across TBX5 Enhancer KO cells (red) and 1000 random samplings of WT late CM cells (gray) (* p <0.05 by Z-test).
K. Dotplot shows the expression of cardiac genes in WT and KO cells belonging to the late CM cluster.

SUPPLEMENTAL FIGURE LEGENDS

Figure S1: Single-cell CRISPRi screen validation and statistics.

A. Brightfield images of H9-dCas9-KRAB cells receiving sgRNAs targeting OCT4 or NT control.
B. (top) OCT4 expression in cells receiving sgRNAs targeting OCT4 or NT control. For both, qPCR quantification normalized to reference gene (RPLP0) and then compared with control cells. (bottom) MALAT1 expression in cells receiving sgRNAs targeting MALAT1 or NT control.
C. Distribution of sgRNA counts in cells with sgRNAs detected.
D. Distribution of cell counts for each sgRNA.
E. Distribution of cell counts for each targeted region.
F. Feature plots of marker genes for neuronal (+SOX2), cardiomyocyte (+TNNT2), mesoderm (+FN1), epithelial (+EPCAM), cardiac fibroblast (+COL3A1), and endoderm cells (+TTR).
G. NGFRAP1 expression in cells receiving sgRNA targeting NGFRAP1 or NT controls (* $p < 0.05$ by Mann-Whitney U).
H. Distribution of cells receiving sgRNAs targeting ZIC2 Promoter or NT controls after differentiation (* $p < 0.05$ by hypergeometric test).
I. TBX5 expression in cells receiving sgRNAs targeting TBX5 Enhancer 3, Enhancer 5, or non-targeting NT control.

Figure S2: Single-cell CRISPRi screen CM subpopulation marker gene expression.

A. Feature plots of marker genes for SOX4+ progenitors, FN1+ early-stage CMs, ACTA2+ mid-stage CMs, and NPPA+ atrial-like late-stage CMs.
B. Example of sgRNA filtering approach. (top) p-Values (hypergeometric test) for late CM depletion for all combinations of 8 sgRNA targeting TNNT2 PROM1. (middle) As above, but sgRNA combinations with TNNT2 PROM1 sgRNA 1 in red. This sgRNA does not bias p-value in either direction and is therefore kept for downstream analysis. (bottom) As above, but sgRNA combinations with TNNT2 PROM1 sgRNA 7 in red. This sgRNA does bias p-values directionally, and is therefore excluded from downstream analysis.
C. To verify that multiple sgRNAs support the same CM differentiation phenotype, we performed n-1 analysis by removing each sgRNA in turn. In this heatmap, the left column represents cells with all sgRNAs targeting an enhancer or promoter. The right columns indicate p-values after removal of cells with individual sgRNAs. (p-values: hypergeometric test).
D. (top) Dotplot shows expression of cardiac genes across CM subpopulations. (bottom) Expression of cardiac genes across CM subpopulations after targeted transcript amplification.
E. Expression of TGFB1 in late CM cells receiving sgRNAs targeting TGFB1 Promoter, Enhancer or NT controls (* $p < 0.05$ by Mann-Whitney U).

Figure S3: Focused screen marker expression and sgRNA distribution.

A. Feature plots of marker genes for neuronal (+SOX2), cardiomyocytes (+TNNT2), endoderm (+TTR).
B. Feature plots of cells receiving sgRNAs targeting TBX5 enhancers (red) or NT control (gray).
C. Differentially expressed genes in cells receiving sgRNAs targeting TBX5 enhancers. Please see description of Manhattan plot in Figure 2I.

Figure S4: Focused screen CM subpopulation marker expression and sgRNA distribution.

A. Feature plots of marker genes for CM progenitors (FN1+), mid CM (ACTA2+), and late CM (NPPA+).
B. Feature plots of cells receiving sgRNAs targeting TBX5 enhancers (red) or NT control (gray).
C. Differentially expressed genes in CM cells receiving sgRNAs targeting TBX5 Enhancers. Please see description of Manhattan plot in Figure 2I.
D. Reclustering of focused screen CM cells through cell label transfer using initial screen as reference.
E. Distribution of cells receiving sgRNAs targeting TBX5 Enhancers across label transferred CM subpopulations (* $p < 0.05$ by hypergeometric test).

Figure S5: TBX5 enhancer knockout cell distribution.

A. UMAP visualization of H9-derived cells after 8 days of differentiation. 5 Louvain clusters indicated.
B. UMAP distribution of TBX5 exon KO and enhancer KO cells after CM differentiation. Shown are two replicate experiments per genotype.
C. PHATE distribution of TBX5 exon and enhancer KO CM differentiation replicate CM cells.
D. Differentially expressed genes in (left) TBX5 exon KO CM cells and (right) TBX5 enhancer 5 KO CM cells.
E. HAS2 transcript expression in exon and enhancer knockout cells after 8 days of CM differentiation. qPCR quantification normalized to reference gene (RPLP0) and then compared with WT cells.

Figure S6: TBX5 heterozygous enhancer knockout validation.

A. Feature plots of marker genes for neuronal (+SOX2), cardiomyocytes (+TNNT2), endoderm (+TTR).
B. Feature plots of TBX5 enhancer 3 (orange), enhancer 5 (yellow) and WT (gray) CMs.
C. Feature plots of HAND1 expression.
D. Reclustering of CM cells from previous datasets through cell label transfer using sequencing exp (Figure 6) as reference.
E. PHATE distribution of CM cells clustered using 4 CM label transfer subpopulations.
F. Distribution of TBX5 enhancer perturbation cells across label transferred CM subpopulations (* $p < 0.05$ by hypergeometric test).
G. Overlap of early CM enriched (left) and late/ven CM depleted (right) hits from original and label transfer clustering of initial screen CMs.

SUPPLEMENTAL TABLE LEGENDS

Table S1: List of target enhancers and sequences used in study.

Table S2: Sequencing statistics.

Table S3: Top 100 Louvain cluster defining genes for each dataset.

Table S4: Differentially expressed genes through hypergeometric test.

Table S5: Focus screen mid-CM and late-CM defining genes.

Table S6: Differentially expressed genes between TBX5 Enhancer5 heterozygous KO cells and WT cells, in the late CM state.

REFERENCES

Agopian, A.J., Goldmuntz, E., Hakonarson, H., Sewda, A., Taylor, D., Mitchell, L.E., and Pediatric Cardiac Genomics Consortium* (2017). Genome-Wide Association Studies and Meta-Analyses for Congenital Heart Defects. Circ. Cardiovasc. Genet. *10*, e001449. .

Basson, C.T., Bachinsky, D.R., Lin, R.C., Levi, T., Elkins, J.A., Soults, J., Grayzel, D., Kroumpouzou, E., Traill, T.A., Leblanc-Straceski, J., et al. (1997). Mutations in human TBX5 [corrected] cause limb and cardiac malformation in Holt-Oram syndrome. Nat. Genet. *15*, 30–35. .

Blue, G.M., Kirk, E.P., Giannoulatou, E., Sholler, G.F., Dunwoodie, S.L., Harvey, R.P., and Winlaw, D.S. (2017). Advances in the Genetics of Congenital Heart Disease: A Clinician's Guide. J. Am. Coll. Cardiol. *69*, 859–870. .

Bruneau, B.G., Logan, M., Davis, N., Levi, T., Tabin, C.J., Seidman, J.G., and Seidman, C.E. (1999). Chamber-Specific Cardiac Expression of Tbx5 and Heart Defects in Holt–Oram Syndrome. Dev. Biol. *211*, 100–108. .

Bruneau, B.G., Nemer, G., Schmitt, J.P., Charron, F., Robitaille, L., Caron, S., Conner, D.A., Gessler, M., Nemer, M., Seidman, C.E., et al. (2001). A murine model of Holt-Oram syndrome defines roles of the T-box transcription factor Tbx5 in cardiogenesis and disease. Cell *106*, 709–721. .

Cadiñanos, J., and Bradley, A. (2007). Generation of an inducible and optimized piggyBac transposon system. Nucleic Acids Res. *35*, e87. .

Castillo-Hair, S.M., Sexton, J.T., Landry, B.P., Olson, E.J., Igoshin, O.A., and Tabor, J.J. (2016). FlowCal: A User-Friendly, Open Source Software Tool for Automatically Converting Flow Cytometry Data from Arbitrary to Calibrated Units. ACS Synth. Biol. *5*, 774–780. .

Cheng, P., Andersen, P., Hassel, D., Kaynak, B.L., Limphong, P., Juergensen, L., Kwon, C., and Srivastava, D. (2013). Fibronectin mediates mesendodermal cell fate decisions. Development *140*, 2587–2596. .

Cordell, H.J., Bentham, J., Topf, A., Zelenika, D., Heath, S., Mamasoula, C., Cosgrove, C., Blue, G., Granados-Riveron, J., Setchfield, K., et al. (2013). Genome-wide association study of multiple congenital heart disease phenotypes identifies a susceptibility locus for atrial septal defect at chromosome 4p16. Nat. Genet. *45*, 822–824. .

Diao, Y., Fang, R., Li, B., Meng, Z., Yu, J., Qiu, Y., Lin, K.C., Huang, H., Liu, T., Marina, R.J., et al. (2017). A tiling-deletion-based genetic screen for cis-regulatory element identification in mammalian cells. Nat. Methods *14*, 629. .

Duan, J., and Hon, G. (2021). FBA: feature barcoding analysis for single cell RNA-Seq. Bioinformatics https://doi.org/10.1093/bioinformatics/btab375.

Fulco, C.P., Munschauer, M., Anyoha, R., Munson, G., Grossman, S.R., Perez, E.M., Kane, M., Cleary, B., Lander, E.S., and Engreitz, J.M. (2016). Systematic mapping of functional enhancer–promoter connections with CRISPR interference. Science *354*, 769–773. .

Fulco, C.P., Nasser, J., Jones, T.R., Munson, G., Bergman, D.T., Subramanian, V., Grossman, S.R., Anyoha, R., Doughty, B.R., Patwardhan, T.A., et al. (2019). Activity-by-contact model of enhancer–promoter regulation from thousands of CRISPR perturbations. Nat. Genet. *51*, 1664–1669. .

Gasperini, M., Findlay, G.M., McKenna, A., Milbank, J.H., Lee, C., Zhang, M.D., Cusanovich, D.A., and Shendure, J. (2017). CRISPR/Cas9-Mediated Scanning for Regulatory Elements Required for HPRT1 Expression via Thousands of Large, Programmed Genomic Deletions. Am. J. Hum. Genet. *101*, 192–205. .

Gasperini, M., Hill, A.J., McFaline-Figueroa, J.L., Martin, B., Kim, S., Zhang, M.D., Jackson, D., Leith, A., Schreiber, J., Noble, W.S., et al. (2019). A Genome-wide Framework for Mapping Gene Regulation via Cellular Genetic Screens. Cell *176*, 1516. .

Genga, R.M.J., Kernfeld, E.M., Parsi, K.M., Parsons, T.J., Ziller, M.J., and Maehr, R. (2019). Single-Cell RNA-Sequencing-Based CRISPRi Screening Resolves Molecular Drivers of Early Human Endoderm Development. Cell Rep. *27*, 708–718.e10. .

Gilsbach, R., Schwaderer, M., Preissl, S., Grüning, B.A., Kranzhöfer, D., Schneider, P., Nührenberg, T.G., Mulero-Navarro, S., Weichenhan, D., Braun, C., et al. (2018). Distinct epigenetic programs regulate cardiac myocyte development and disease in the human heart in vivo. Nat. Commun. *9*, 391. .

Hoffman, J.I.E., and Kaplan, S. (2002). The incidence of congenital heart disease. J. Am. Coll. Cardiol. *39*, 1890–1900. .

Holt, M., and Oram, S. (1960). Familial heart disease with skeletal malformations. Br. Heart J. *22*, 236–242. .

van den Hoogenhof, M.M.G., Beqqali, A., Amin, A.S., van der Made, I., Aufiero, S., Khan, M.A.F., Schumacher, C.A., Jansweijer, J.A., van Spaendonck-Zwarts, K.Y., Remme, C.A., et al. (2018). RBM20 Mutations Induce an Arrhythmogenic Dilated Cardiomyopathy Related to Disturbed Calcium Handling. Circulation *138*, 1330–1342. .

Houweling, A.C., van Borren, M.M., Moorman, A.F.M., and Christoffels, V.M. (2005). Expression and regulation of the atrial natriuretic factor encoding gene Nppa during development and disease. Cardiovasc. Res. *67*, 583–593. .

Kathiriya, I.S., Rao, K.S., Iacono, G., Devine, W.P., Blair, A.P., Hota, S.K., Lai, M.H., Garay, B.I., Thomas, R., Gong, H.Z., et al. (2021). Modeling Human TBX5 Haploinsufficiency Predicts Regulatory Networks for Congenital Heart Disease. Dev. Cell *56*, 292–309.e9. .

Klann, T.S., Barrera, A., Ettyreddy, A.R., Rickels, R.A., Bryois, J., Jiang, S., Adkar, S.S., Iglesias, N., Sullivan, P.F., Reddy, T.E., et al. (2021). Genome-wide annotation of gene regulatory elements linked to cell fitness.

Li, Q.Y., Newbury-Ecob, R.A., Terrett, J.A., Wilson, D.I., Curtis, A.R., Yi, C.H., Gebuhr, T., Bullen, P.J., Robson, S.C., Strachan, T., et al. (1997). Holt-Oram syndrome is caused by mutations in TBX5, a member of the Brachyury (T) gene family. Nat. Genet. *15*, 21–29. .

van der Linde, D., Konings, E.E.M., Slager, M.A., Witsenburg, M., Helbing, W.A., Takkenberg, J.J.M., and Roos-Hesselink, J.W. (2011). Birth prevalence of congenital heart disease

worldwide: a systematic review and meta-analysis. J. Am. Coll. Cardiol. *58*, 2241–2247. .

Liu, Q., Jiang, C., Xu, J., Zhao, M.-T., Van Bortle, K., Cheng, X., Wang, G., Chang, H.Y., Wu, J.C., and Snyder, M.P. (2017). Genome-Wide Temporal Profiling of Transcriptome and Open Chromatin of Early Cardiomyocyte Differentiation Derived From hiPSCs and hESCs. Circ. Res. *121*, 376–391. .

Luo, Z., Gao, X., Lin, C., Smith, E.R., Marshall, S.A., Swanson, S.K., Florens, L., Washburn, M.P., and Shilatifard, A. (2015). Zic2 is an enhancer-binding factor required for embryonic stem cell specification. Mol. Cell *57*, 685–694. .

Macosko, E.Z., Basu, A., Satija, R., Nemesh, J., Shekhar, K., Goldman, M., Tirosh, I., Bialas, A.R., Kamitaki, N., Martersteck, E.M., et al. (2015). Highly Parallel Genome-wide Expression Profiling of Individual Cells Using Nanoliter Droplets. Cell *161*, 1202–1214. .

van Nieuwenhoven, F.A., Hemmings, K.E., Porter, K.E., and Turner, N.A. (2013). Combined effects of interleukin-1α and transforming growth factor-β1 on modulation of human cardiac fibroblast function. Matrix Biol. *32*, 399–406. .

Paul, M.H., Harvey, R.P., Wegner, M., and Sock, E. (2014). Cardiac outflow tract development relies on the complex function of Sox4 and Sox11 in multiple cell types. Cell. Mol. Life Sci. *71*, 2931–2945. .

Plank, J.L., and Dean, A. (2014). Enhancer function: mechanistic and genome-wide insights come together. Mol. Cell *55*, 5–14. .

Potta, S.P., Liang, H., Winkler, J., Doss, M.X., Chen, S., Wagh, V., Pfannkuche, K., Hescheler, J., and Sachinidis, A. (2010). Isolation and Functional Characterization of α-Smooth Muscle Actin Expressing Cardiomyocytes from Embryonic Stem Cells. Cell. Physiol. Biochem. *25*, 595–604. .

Reilly, S.K., Gosai, S.J., Gutierrez, A., Mackay-Smith, A., Ulirsch, J.C., Kanai, M., Mouri, K., Berenzy, D., Kales, S., Butler, G.M., et al. (2021). Direct characterization of cis-regulatory elements and functional dissection of complex genetic associations using HCR–FlowFISH. Nat. Genet. *53*, 1166–1176. .

Replogle, J.M., Saunders, R.A., Pogson, A.N., Hussmann, J.A., Lenail, A., Guna, A., Mascibroda, L., Wagner, E.J., Adelman, K., Lithwick-Yanai, G., et al. (2022). Mapping information-rich genotype-phenotype landscapes with genome-scale Perturb-seq. Cell *185*, 2559–2575.e28. .

Richter, F., Morton, S.U., Kim, S.W., Kitaygorodsky, A., Wasson, L.K., Chen, K.M., Zhou, J., Qi, H., Patel, N., DePalma, S.R., et al. (2020). Genomic analyses implicate noncoding de novo variants in congenital heart disease. Nat. Genet. https://doi.org/10.1038/s41588-020-0652-z.

Siepel, A., Bejerano, G., Pedersen, J.S., Hinrichs, A.S., Hou, M., Rosenbloom, K., Clawson, H., Spieth, J., Hillier, L.W., Richards, S., et al. (2005). Evolutionarily conserved elements in vertebrate, insect, worm, and yeast genomes. Genome Res. *15*, 1034–1050. .

Smemo, S., Campos, L.C., Moskowitz, I.P., Krieger, J.E., Pereira, A.C., and Nobrega, M.A. (2012). Regulatory variation in a TBX5 enhancer leads to isolated congenital heart disease. Hum. Mol. Genet. *21*, 3255–3263. .

Steimle, J.D., and Moskowitz, I.P. (2017). TBX5: A Key Regulator of Heart Development. Curr. Top. Dev. Biol. *122*, 195–221. .

Stoeckius, M., Zheng, S., Houck-Loomis, B., Hao, S., Yeung, B.Z., Mauck, W.M., 3rd, Smibert, P., and Satija, R. (2018). Cell Hashing with barcoded antibodies enables multiplexing and doublet detection for single cell genomics. Genome Biol. *19*, 224. .

Thakore, P.I., D'Ippolito, A.M., Song, L., Safi, A., Shivakumar, N.K., Kabadi, A.M., Reddy, T.E., Crawford, G.E., and Gersbach, C.A. (2015). Highly specific epigenome editing by CRISPR-Cas9 repressors for silencing of distal regulatory elements. Nat. Methods *12*, 1143–1149. .

Tian, R., Gachechiladze, M.A., Ludwig, C.H., Laurie, M.T., Hong, J.Y., Nathaniel, D., Prabhu, A.V., Fernandopulle, M.S., Patel, R., Abshari, M., et al. (2019). CRISPR Interference-Based Platform for Multimodal Genetic Screens in Human iPSC-Derived Neurons. Neuron *104*, 239–255.e12. .

Tohyama, S., Hattori, F., Sano, M., Hishiki, T., Nagahata, Y., Matsuura, T., Hashimoto, H., Suzuki, T., Yamashita, H., Satoh, Y., et al. (2013). Distinct metabolic flow enables large-scale purification of mouse and human pluripotent stem cell-derived cardiomyocytes. Cell Stem Cell *12*, 127–137. .

Tompkins, J.D., Jung, M., Chen, C.-Y., Lin, Z., Ye, J., Godatha, S., Lizhar, E., Wu, X., Hsu, D., Couture, L.A., et al. (2016). Mapping Human Pluripotent-to-Cardiomyocyte Differentiation: Methylomes, Transcriptomes, and Exon DNA Methylation "Memories." EBioMedicine *4*, 74–85. .

Wolf, F.A., Angerer, P., and Theis, F.J. (2018). SCANPY: large-scale single-cell gene expression data analysis. Genome Biol. *19*, 15. .

Xie, S., Duan, J., Li, B., Zhou, P., and Hon, G.C. (2017). Multiplexed Engineering and Analysis of Combinatorial Enhancer Activity in Single Cells. Mol. Cell *66*, 285–299.e5. .

Xie, S., Armendariz, D., Zhou, P., Duan, J., and Hon, G.C. (2019). Global Analysis of Enhancer Targets Reveals Convergent Enhancer-Driven Regulatory Modules. Cell Rep. *29*, 2570–2578.e5. .

Xu, J., Zhou, C., Foo, K.S., Yang, R., Xiao, Y., Bylund, K., Sahara, M., and Chien, K.R. (2020). Genome-wide CRISPR screen identifies ZIC2 as an essential gene that controls the cell fate of early mesodermal precursors to human heart progenitors. Stem Cells *38*, 741–755. .

Zhang, Y., Li, T., Preissl, S., Amaral, M.L., Grinstein, J.D., Farah, E.N., Destici, E., Qiu, Y., Hu, R., Lee, A.Y., et al. (2019). Transcriptionally active HERV-H retrotransposons demarcate topologically associating domains in human pluripotent stem cells. Nat. Genet. *51*, 1380–1388. .

Zhao, T., Bai, R., Wu, F., Lu, W.-J., and Zhang, J. (2021). Generation of a TBX5 homozygous knockout embryonic stem cell line (WAe009-A-45) by CRISPR/Cas9 genome editing. Stem Cell Res. *51*, 102156. .

Zhou, H.Y., Katsman, Y., Dhaliwal, N.K., Davidson, S., Macpherson, N.N., Sakthidevi, M., Collura, F., and Mitchell, J.A. (2014). A Sox2 distal enhancer cluster regulates embryonic stem cell differentiation potential. Genes Dev. *28*, 2699–2711. .

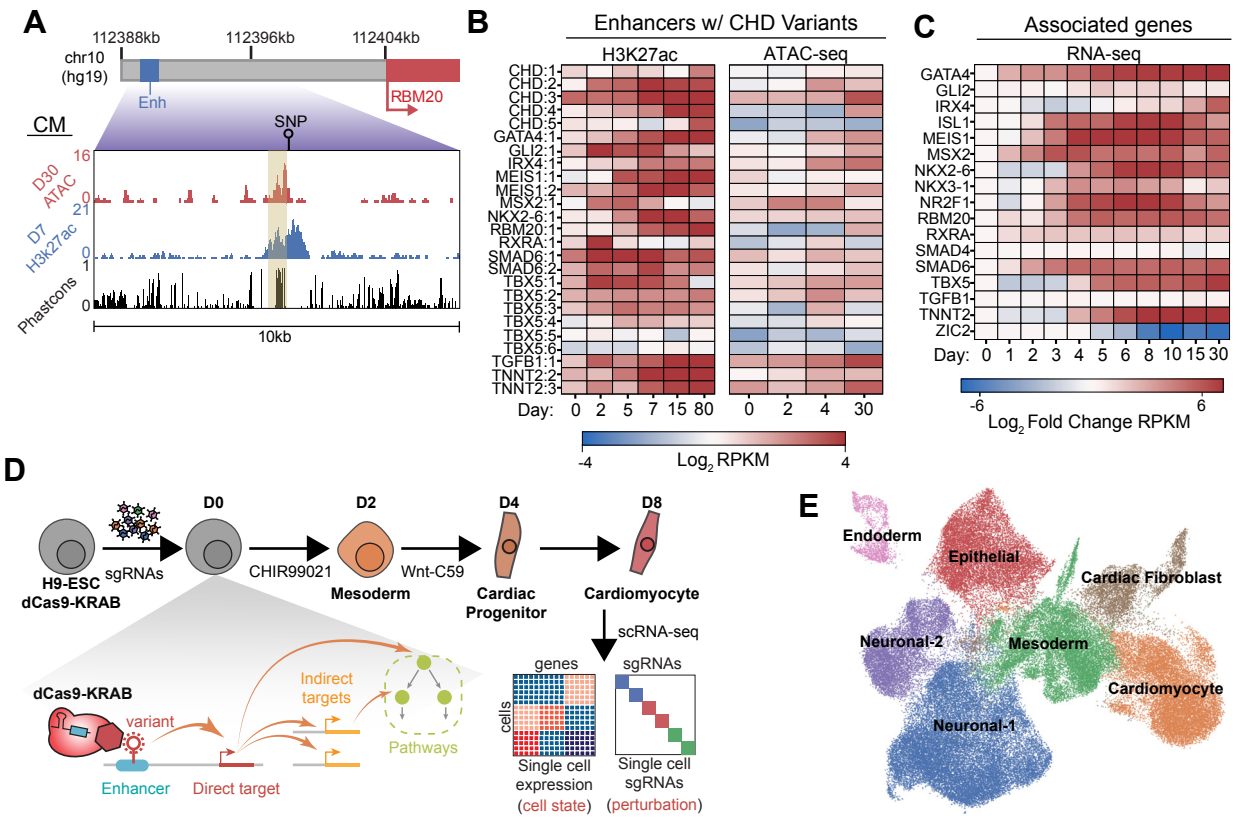

Figure 1: Single-cell screens of CHD-associated enhancers during cardiomyocyte differentiation.

A. Genome browser snapshot emphasizing features of a targeted enhancer about 15kb upstream of the RBM20 gene. Yellow highlights enhancer region.

B. H3K27ac and open chromatin (ATAC-Seq) enrichment for targeted enhancers across multiple timepoints of CM differentiation (Liu et al., 2017; Tompkins et al., 2016; Zhang et al., 2019).

C. Expression of putative target genes across multiple stages of CM differentiation. Expression defined as fold change over the day 0 expression of a target gene (Tompkins et al., 2016).

D. Schematic of single-cell CRISPRi screen. H9-dCas9-KRAB cells are infected with a lentiviral sgRNA library and differentiated over 8 days into CMs followed by scRNA-seq. Individual cells are linked to sgRNA perturbations and changes in transcriptional cell state.

E. UMAP visualization of H9-derived cells after 8 days of differentiation. 7 Louvain clusters indicated.

F. Expression of the top 100 cluster defining genes for each Louvain cluster cell type.

G. MALAT1 expression in control (non-targeting) and sgMALAT1 cells (* p < 0.05 by Mann-Whitney U).

H. Distribution of cells receiving sgNT, sgTBX5 PROM1, sgTBX5 ENH6 that differentiate into CM and mesoderm states (* p <0.05 and ** p <0.0008 by hypergeometric test).

Figure 2

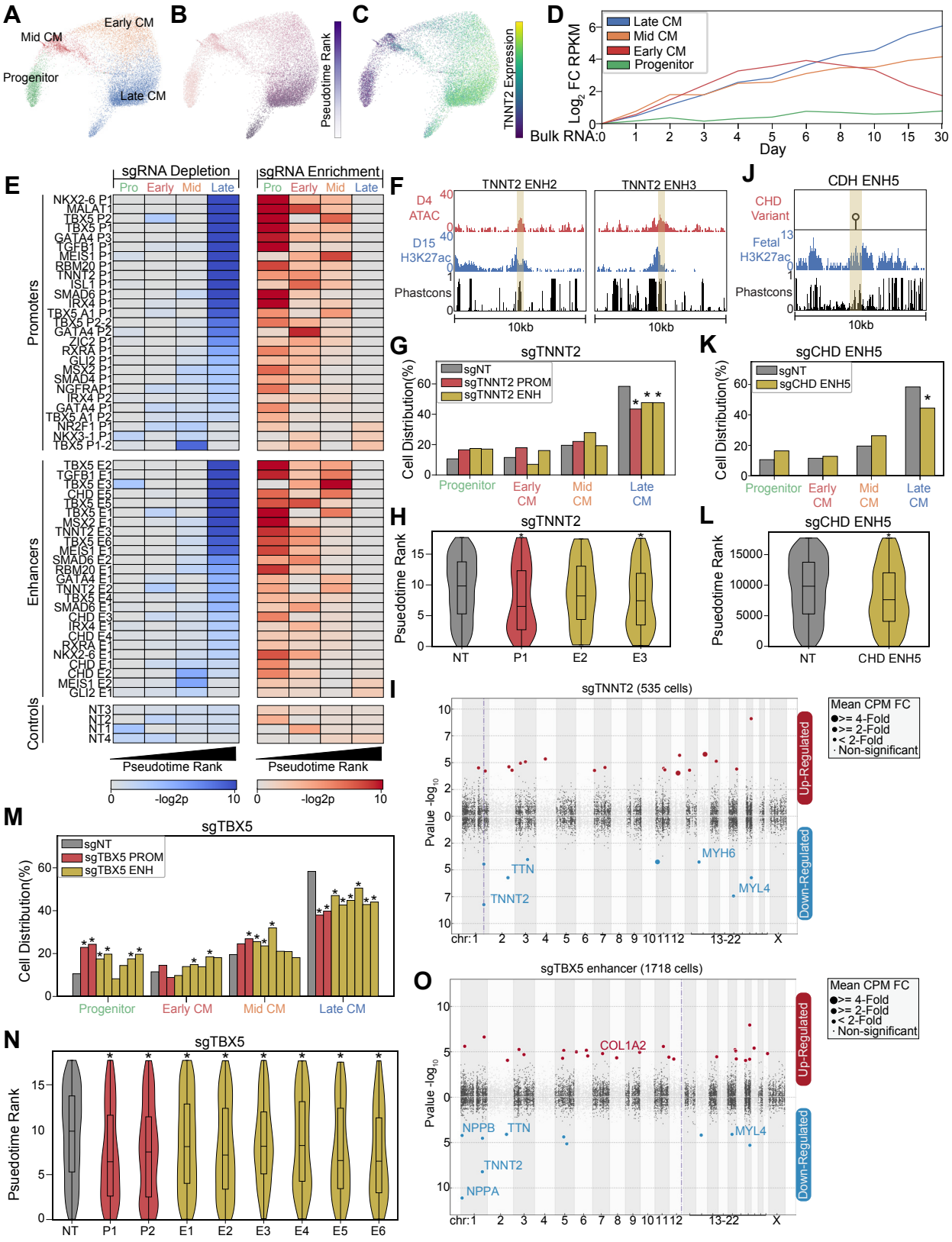

Figure 2: CRISPRi of CHD-associated enhancers delays cardiomyocyte differentiation.

A. PHATE visualization of CM cells with 4 Louvain clusters.

B. Feature plot of pseudotime ranking of cells across PHATE trajectory.

C. Feature plot of TNNT2 expression.

D. We defined the top 100 genes for each of the 4 CM subtypes. Shown is the expression of these gene sets in bulk RNA-Seq experiments of CM differentiation (Tompkins et al., 2016). Expression defined as fold change over day 0.

E. Enrichment (right) and depletion (left) of cells with distinct perturbations across CM sub-populations (p-values: hypergeometric test). Top: Targeted promoters; middle: targeted enhancers; bottom: non-targeting sgRNAs.

F. Genome browser tracks of chromatin and sequence conservation at two putative TNNT2 enhancers (ENH2 and ENH3). Yellow region denotes enhancer boundaries.

G. Distribution of states for cells receiving sgRNAs targeting TNNT2 promoter and enhancers (* $p < 0.05$ by hypergeometric test).

H. Distribution of pseudotime rank for cells receiving sgRNAs targeting TNNT2 promoter and enhancers (* $p < 0.05$ by Mann-Whitney U).

I. Differentially expressed genes in CM cells receiving sgRNAs targeting TNNT2 promoter or enhancers. In this Manhattan plot, the horizontal axis indicates genomic coordinates, with the dotted line indicating the targeted TNNT2 promoter. The vertical axis indicates differential expression (p-value), with positive values representing increased expression and negative values representing decreased expression.

J. Genome browser track of fetal human heart H3K27ac for CHD ENH5. Yellow region denotes enhancer boundaries.

K. Distribution of states for cells receiving sgRNAs targeting CHD ENH5 (* $p < 0.05$ by hypergeometric test).

L. Distribution of pseudotime rank for cells receiving sgRNAs targeting CHD ENH5 (* $p < 0.05$ by Mann-Whitney U).

M. Distribution of states for cells receiving sgRNAs targeting TBX5 promoters and enhancers (* $p < 0.05$ by hypergeometric test).

N. Distribution of pseudotime rank for cells receiving sgRNAs targeting TBX5 promoter and enhancers (* $p < 0.05$ by Mann-Whitney U).

O. Differentially expressed genes in CM cells receiving sgRNAs targeting a TBX5 enhancer (as described in 2I).

Figure 3

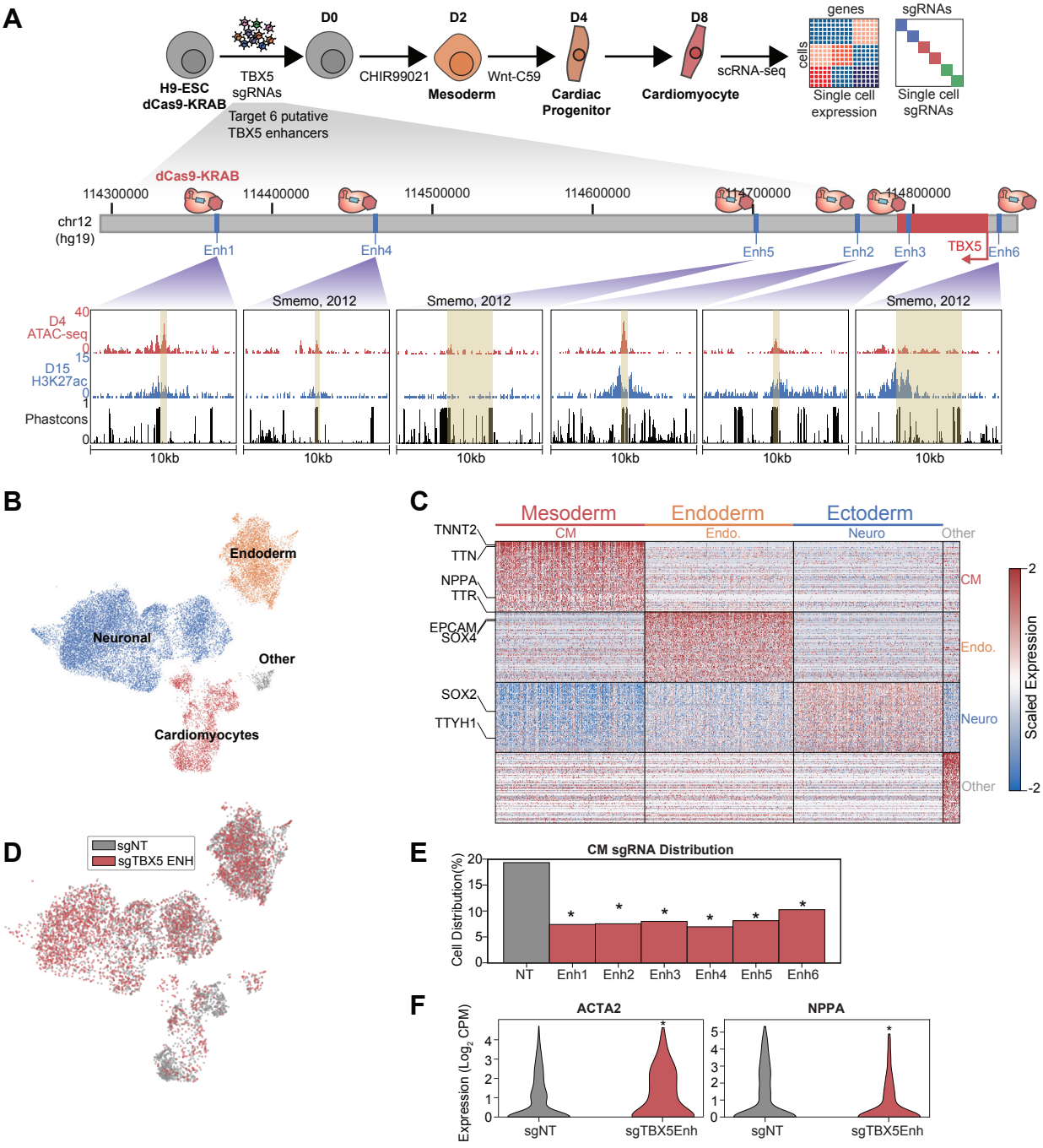

Figure 3: A focused validation screen demonstrates that TBX5 enhancers modulate CM cell fate.

A. (Top) Schematic of validation CRISPRi screen. H9-dCas9-KRAB cells are infected with lentiviral sgRNA library targeting TBX5 enhancers and differentiated over 8 days into CMs followed by scRNA-seq. (Bottom) Genome browser tracks of chromatin status and sequence conservation for TBX5 enhancers. Yellow regions denote enhancers.

B. UMAP visualization of H9-derived cells after 8 days of differentiation. 4 Louvain clusters indicated.

C. Expression of the top 100 cluster-defining genes for each Louvain cluster.

D. Feature plots of cells receiving sgRNAs targeting TBX5 enhancers (red) or non-targeting (NT) control (gray).

E. Distribution of cells receiving sgNT and sgTBX5 enhancers that differentiate into CMs (* $p < 0.05$ by hypergeometric test).

F. Expression of ACTA2 (left) and NPPA (right) in sgTBX5 enhancer and control sgNT CMs (* $p < 0.05$ by Mann-Whitney U).

Figure 4

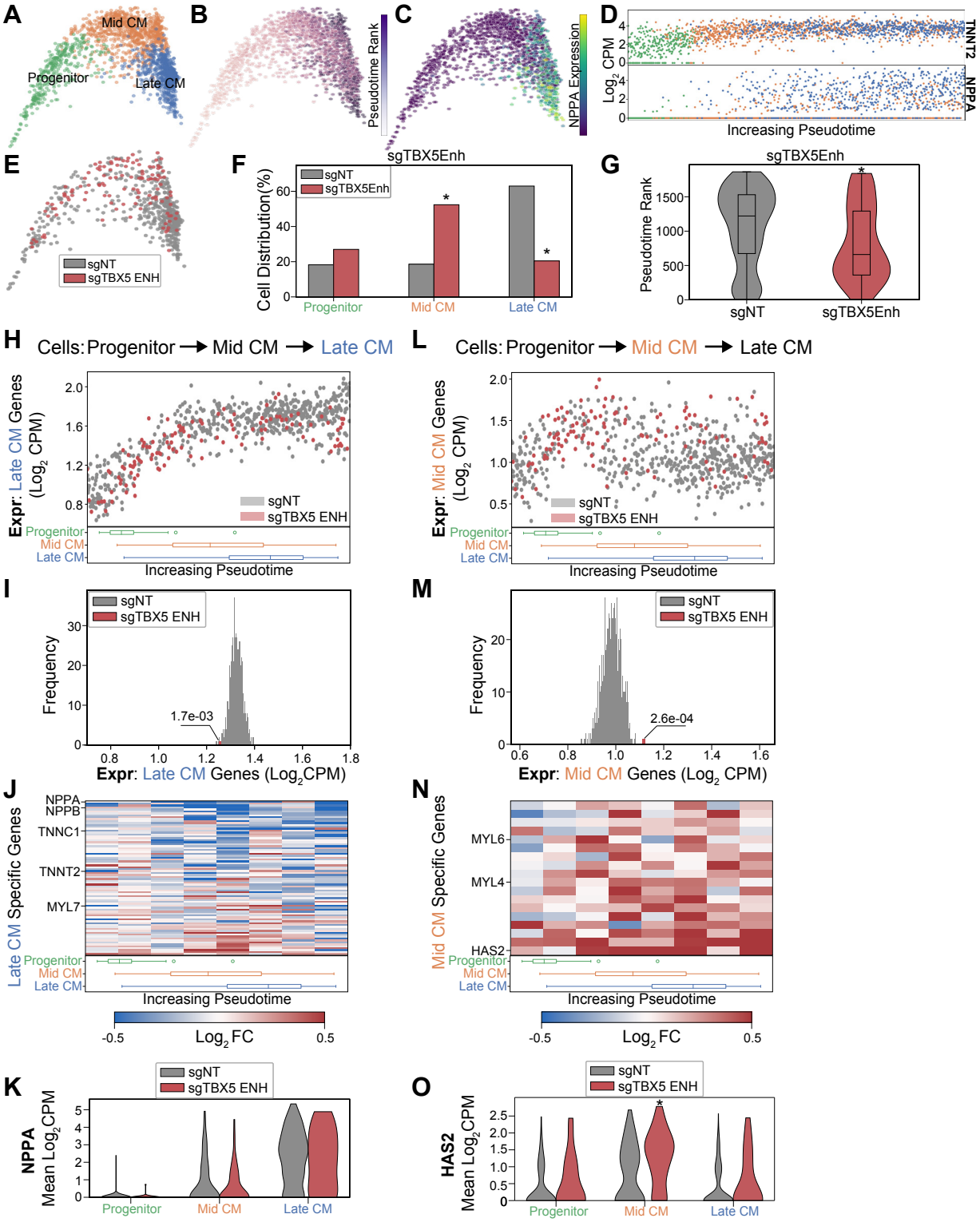

Figure 4: TBX5 enhancer repression alters CM molecular signatures.

A. PHATE visualization of CMs in the focused screen with 3 Louvain clusters.

B. Feature plot of pseudotime ranking of cells across PHATE trajectory.

C. Feature plot of NPPA expression.

D. Single-cell expression of TNNT2 (top) and NPPA (bottom) across pseudotime ordered CMs.

E. Feature plots of cells receiving sgRNAs targeting TBX5 enhancers or non-targeting NT control.

F. Distribution of states for cells receiving sgRNAs targeting TBX5 enhancers or non-targeting NT control (* $p < 0.05$ by hypergeometric test).

G. Distribution of pseudotime rank for cells receiving sgRNAs targeting TBX5 enhancers and NCs (* $p < 0.05$ by Mann-Whitney U).

H. (top) We defined late CM genes as those more expressed in late CM cells. Shown is the average expression of late CM genes in cells across pseudotime. Cells receiving sgRNAs targeting TBX5 enhancers (red) or non-targeting NT control (gray). (bottom) Boxplots of CM subpopulation pseudotime ranks across pseudotime.

I. Average expression of late CM genes across cells receiving sgRNAs targeting TBX5 enhancers (red) and 1000 random samplings of non-targeting control (sgNT) late CM cells (gray) (* $p < 0.05$ by Z-test).

J. (top) For late CM genes, shown is the relative expression in cells receiving sgRNAs targeting TBX5 enhancers compared with non-targeting NT control, across pseudotime. (bottom) Boxplots of CM subpopulation pseudotime ranks across pseudotime.

K. NPPA expression in cells receiving sgRNAs targeting TBX5 enhancers and NC.

L. (top) We defined mid CM genes as those more expressed in mid CM cells. Shown is the average expression of mid CM genes in cells across pseudotime. Cells receiving sgRNAs targeting TBX5 enhancers (red) or non-targeting NT control (gray). (bottom) Boxplots of CM subpopulation pseudotime ranks across pseudotime.

M. Averaged expression of mid CM genes across cells receiving sgRNAs targeting TBX5 enhancers (red) and 1000 random samplings of non-targeting control (sgNT) late CM cells (gray) (* $p < 0.05$ by Z-test).

N. (top) For mid CM genes, shown is the relative expression in cells receiving sgRNAs targeting TBX5 enhancers compared with non-targeting NT control, across pseudotime. (bottom) Boxplots of CM subpopulation pseudotime ranks across pseudotime.

O. HAS2 expression in cells receiving sgRNAs targeting TBX5 enhancers and non-targeting NT control.

Figure 5: TBX5 enhancer knockout induces CHD phenotypes.

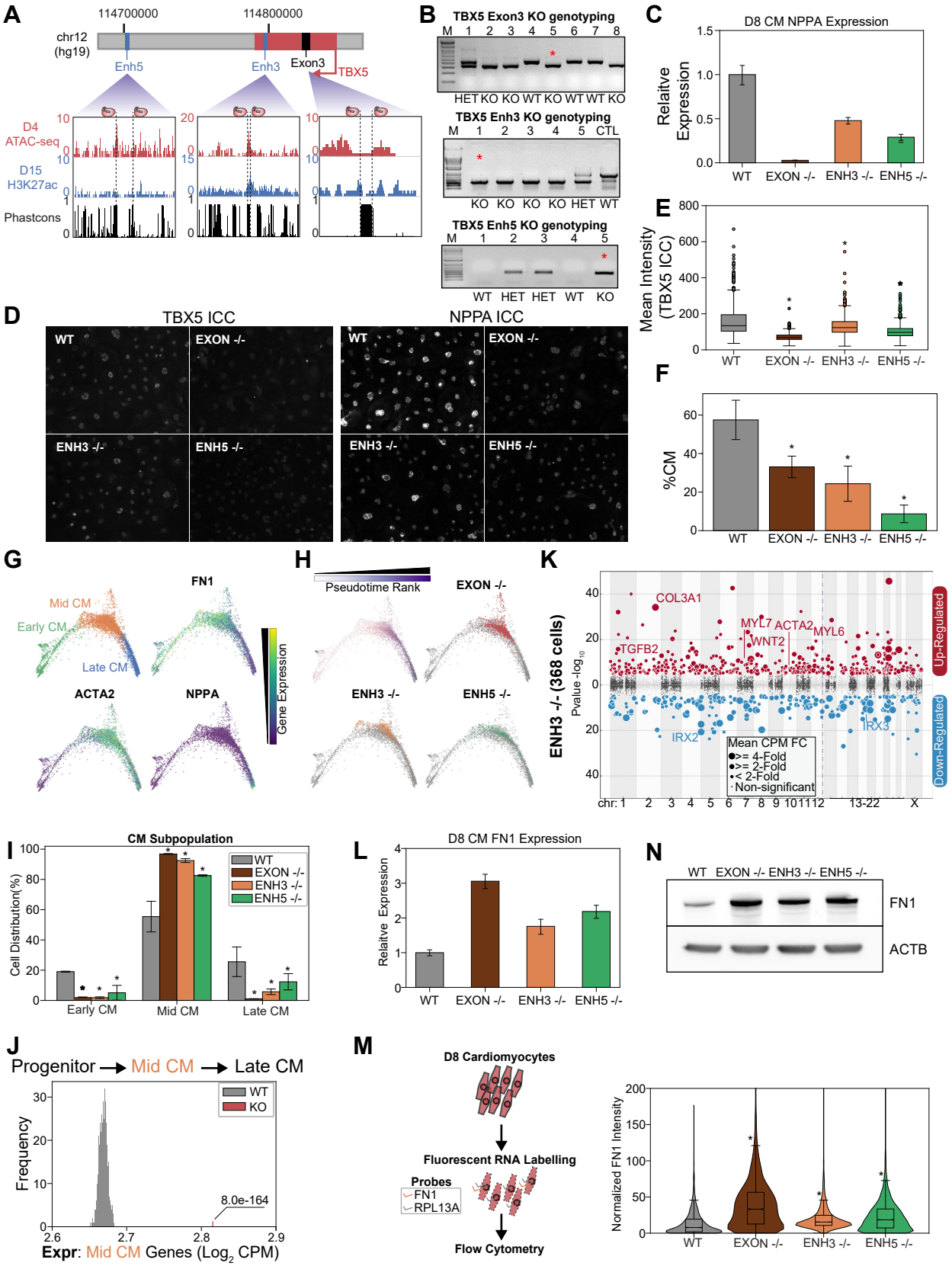

Figure 5: TBX5 enhancer knockouts recapitulate CRISPRi phenotypes.

A. (top) TBX5 enhancer knockout strategy. (bottom) Genome browser snapshots of chromatin status and sequence conservation. Dotted lines denote sgRNA target sites.

B. Genotyping PCR to verify TBX5 knockouts of exon 3 (top), enhancer 3 (middle), and enhancer 5 (bottom). Red asterisk indicates clones used in downstream analysis.

C. NPPA transcript expression in exon and enhancer knockout cells after 8 days of CM differentiation. qPCR quantification normalized to reference gene (RPLP0) and then compared with WT cells.

D. ICC for TBX5 (left) and NPPA (right) in WT and TBX5 exon 3, enhancer 3, and enhancer 5 knockout cells.

E. Quantification of TBX5 ICC (mean intensity) across TBX5 genotyping (* $p < 0.05$ by Mann-Whitney U).

F. Distribution of WT, TBX5 enhancer KO, or exon KO cells that differentiate into CMs relative to endoderm population (* $p < 0.05$ by hypergeometric test).

G. (top left) PHATE visualization of CMs with 3 Louvain clusters. (other quadrants) Feature plots of FN1, ACTA2, and NPPA expression.

H. (top left) Feature plot of pseudotime ranking of CM cells across PHATE trajectory. (other quadrants) Distribution of TBX5 exon KO and enhancer KO cells across CM trajectory. WT: gray.

I. Distribution of WT, TBX5 exon KO, and enhancer KO cells across 3 CM subpopulations (* $p < 0.05$ by hypergeometric test).

J. Averaged expression of mid CM genes across TBX5 exon and enhancer KO cells (red) and 1000 random samplings of WT mid CM cells (gray) (* $p < 0.05$ by Z-test).

K. Differentially expressed genes in enhancer 3 KO cells in CM states. Please see description of Manhattan plot in Figure 2I.

L. FN1 transcript expression in exon and enhancer knockout cells after 8 days of CM differentiation. qPCR quantification normalized to reference gene (RPLP0) and then compared with WT cells.

M. (left) Overview of FlowFISH experiment. (right) Flow cytometry of FN1 RNA FISH intensity normalized by control RPL13A intensity in TBX5 WT and KO lines (* $p < 0.05$ by Mann-Whitney U).

N. (top) FN1 and ACTB (bottom) protein expression in WT, TBX5 exon and enhancer KO cells after 8 days of CM differentiation.

Figure 6

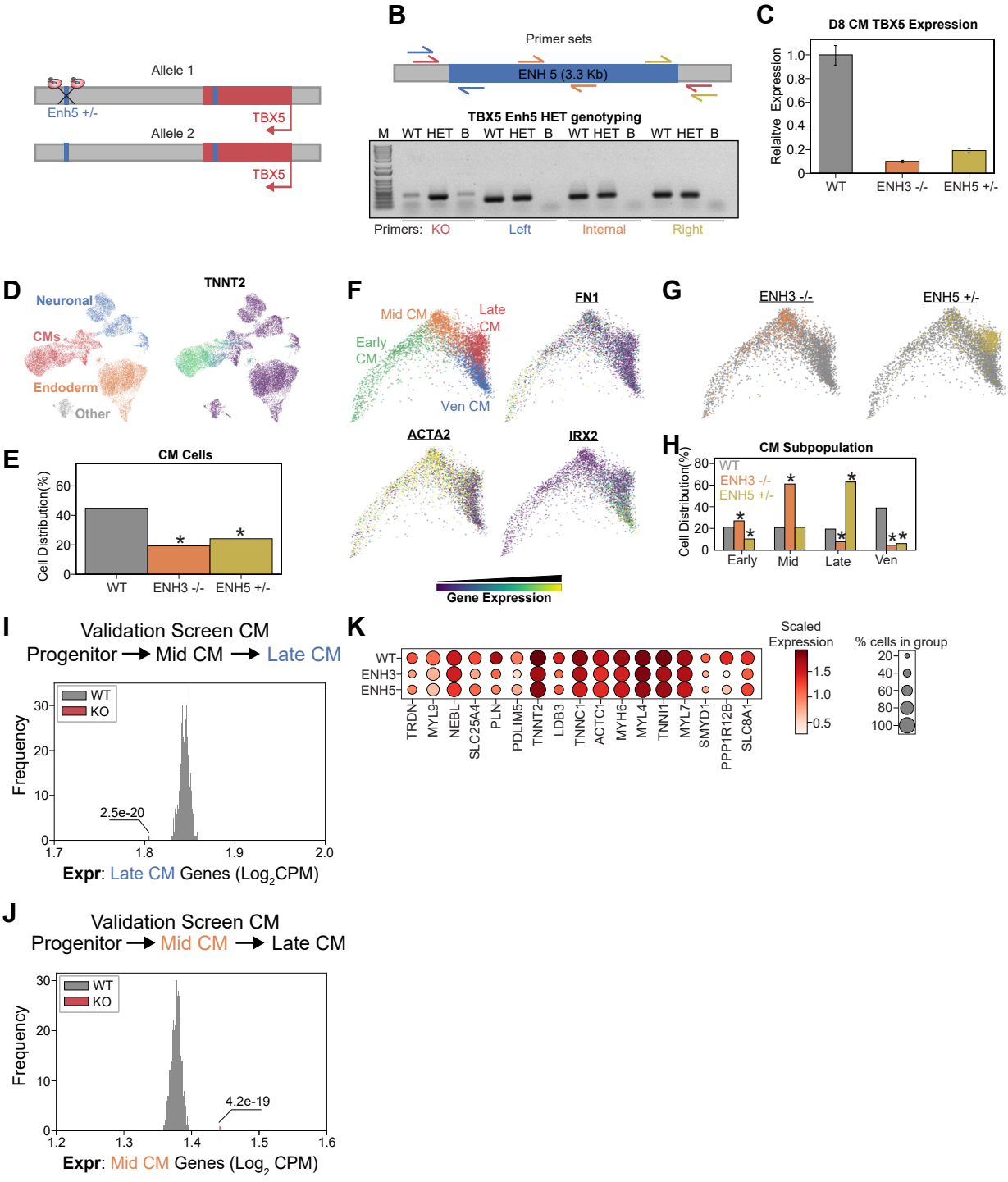

Figure 6: Heterozygous TBX5 enhancer 5 knockout displays reduced phenotypes.

A. TBX5 enhancer 5 heterozygous knockout strategy.

B. (top) Position of primers used to validate TBX5 enhancer 5 heterozygous clone. Red: KO enhancer-spanning primers; blue: left junction primers; orange: enhancer internal primers; and yellow: right junction primers. (bottom) Genotyping PCR to verify TBX5 enhancer 5 heterozygous deletion. Like the WT, the heterozygous clone retains left, internal, and right fragments, consistent with retaining a copy of enhancer 5. Unlike the WT, the heterozygous clone yields a small fragment when amplified with the KO enhancer-spanning primers. PCR conditions were not optimized for amplification of the WT large 3-kb+ fragment. WT: wild-type; HET: TBX5 enhancer 5 heterozygous clone; B: blank.

C. TBX5 transcript expression in enhancer knockout cells after 8 days of CM differentiation. qPCR quantification normalized to reference gene (RPLP0) and then compared with control cells.

D. (left) UMAP visualization of H9-derived cells after 8 days of differentiation. 4 Louvain clusters indicated. (right) Feature plot of TNNT2 expression.

E. Distribution of WT and TBX5 Enhancer KO cells after differentiation (* $p < 0.05$ by hypergeometric test).

F. (top left) PHATE visualization of CM trajectory cells with 4 distinct Louvain clusters. (other quadrants) Feature plot of FN1, ACTA2, and IRX2 expression.

G. Distribution of TBX5 Enhancer KO cells across CM trajectory. WT: gray.

H. Cell distribution of TBX5 Enhancer KO cells across 4 CM subpopulations. (* $p < 0.05$ by hypergeometric test).

I. Averaged expression of late CM genes across TBX5 Enhancer KO cells (red) and 1000 random samplings of WT late CM cells (gray) (* $p < 0.05$ by Z-test).

J. Averaged expression of mid CM genes across TBX5 Enhancer KO cells (red) and 1000 random samplings of WT late CM cells (gray) (* $p < 0.05$ by Z-test).

K. Dotplot shows the expression of cardiac genes in WT and KO cells belonging to the late CM cluster.

Figure S1

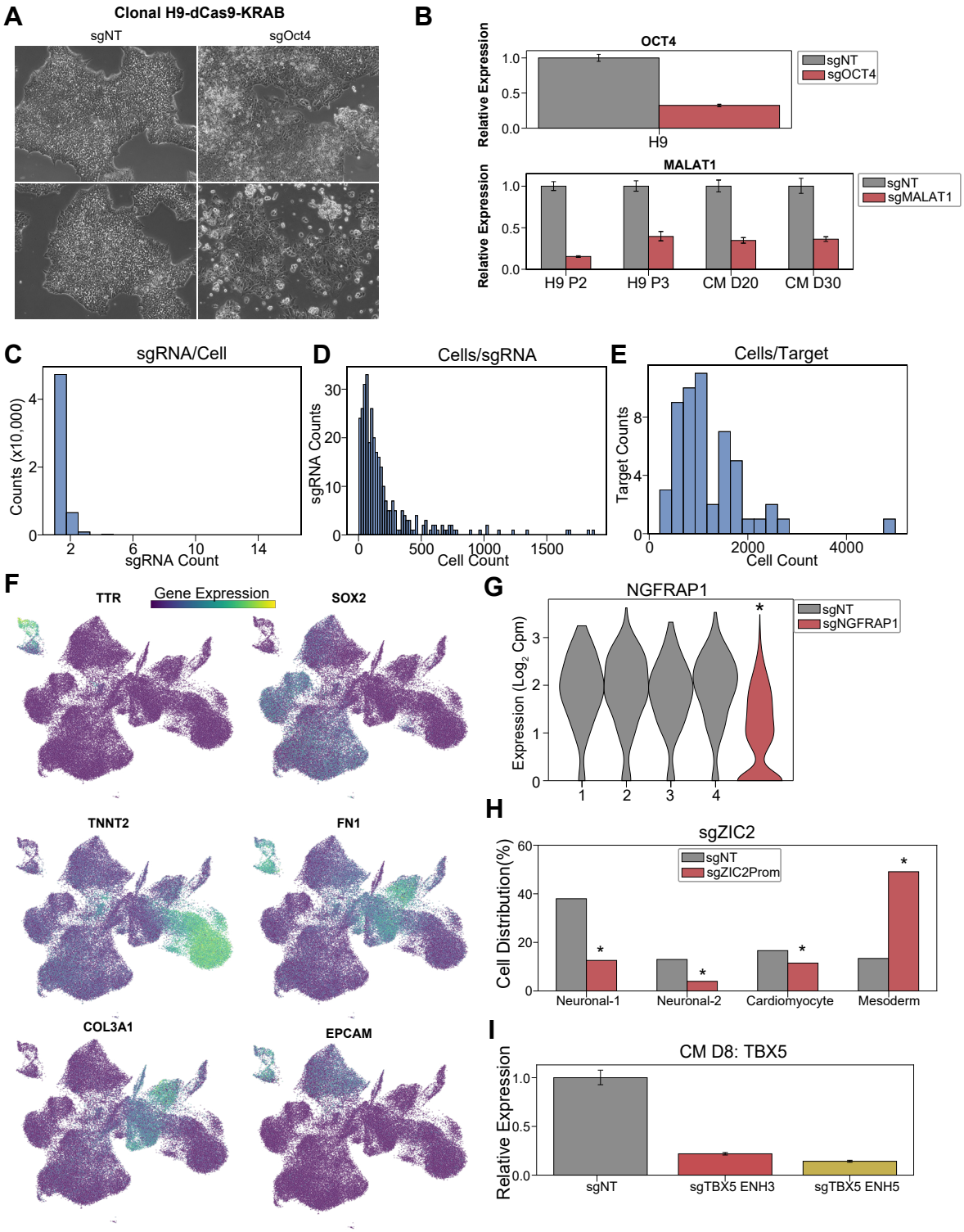

Figure S1: Single-cell CRISPRi screen validation and statistics.

A. Brightfield images of H9-dCas9-KRAB cells receiving sgRNA targeting OCT4 or NT control.

B. (top) OCT4 expression in cells receiving sgRNAs targeting OCT4 or NT control. For both, qPCR quantification normalized to reference gene (RPLP0) and then compared with control cells. (bottom) MALAT1 expression in cells receiving sgRNAs targeting MALAT1 or NT control.

C. Distribution of sgRNA counts in cells with sgRNAs detected.

D. Distribution of cell counts for each sgRNA.

E. Distribution of cell counts for each targeted region.

F. Feature plots of marker genes for neuronal (+SOX2), cardiomyocyte (+TNNT2), mesoderm (+FN1), epithelial (+EPCAM), cardiac fibroblast (+COL3A1), and endoderm cells (+TTR).

G. NGFRAP1 expression in cells receiving sgRNA targeting NGFRAP1 or NT controls (* $p < 0.05$ by Mann-Whitney U).

H. Distribution of cells receiving sgRNAs targeting ZIC2 Promoter or NT controls after differentiation (* $p < 0.05$ by hypergeometric test).

I. TBX5 expression in cells receiving sgRNAs targeting TBX5 Enhancer 3, Enhancer 5, or non-targeting NT control.

Figure S2

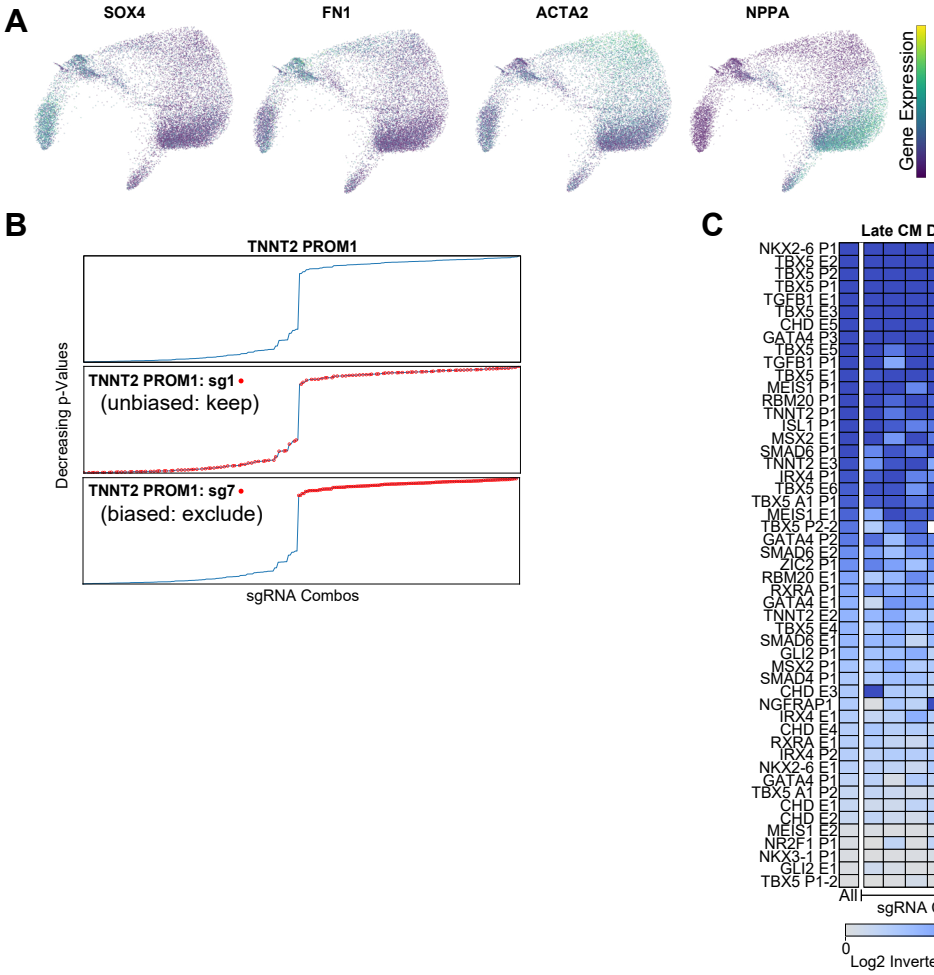

Figure S2: Single-cell CRISPRi screen CM subpopulation marker gene expression.

A. Feature plots of marker genes for SOX4+ progenitors, FN1+ early-stage CMs, ACTA2+ mid-stage CMs, and NPPA+ atrial-like late-stage CMs.

B. Example of sgRNA filtering approach. (top) p-Values (hypergeometric test) for late CM depletion for all combinations of 8 sgRNA targeting TNNT2 PROM1. (middle) As above, but sgRNA combinations with TNNT2 PROM1 sgRNA 1 in red. This sgRNA does not bias p-value in either direction and is therefore kept for downstream analysis. (bottom) As above, but sgRNA combinations with TNNT2 PROM1 sgRNA 7 in red. This sgRNA does bias p-values directionally, and is therefore excluded from downstream analysis.

C. To verify that multiple sgRNAs support the same CM differentiation phenotype, we performed n-1 analysis by removing each sgRNA in turn. In this heatmap, the left column represents cells with all sgRNAs targeting an enhancer or promoter. The right columns indicate p-values after removal of cells with individual sgRNAs. (p-values: hypergeometric test).

D. (top) Dotplot shows expression of cardiac genes across CM subpopulations. (bottom) Expression of cardiac genes across CM subpopulations after targeted transcript amplification.

E. Expression of TGFB1 in late CM cells receiving sgRNAs targeting TGFB1 Promoter, Enhancer or NT controls (* $p < 0.05$ by Mann-Whitney U).

Figure S3

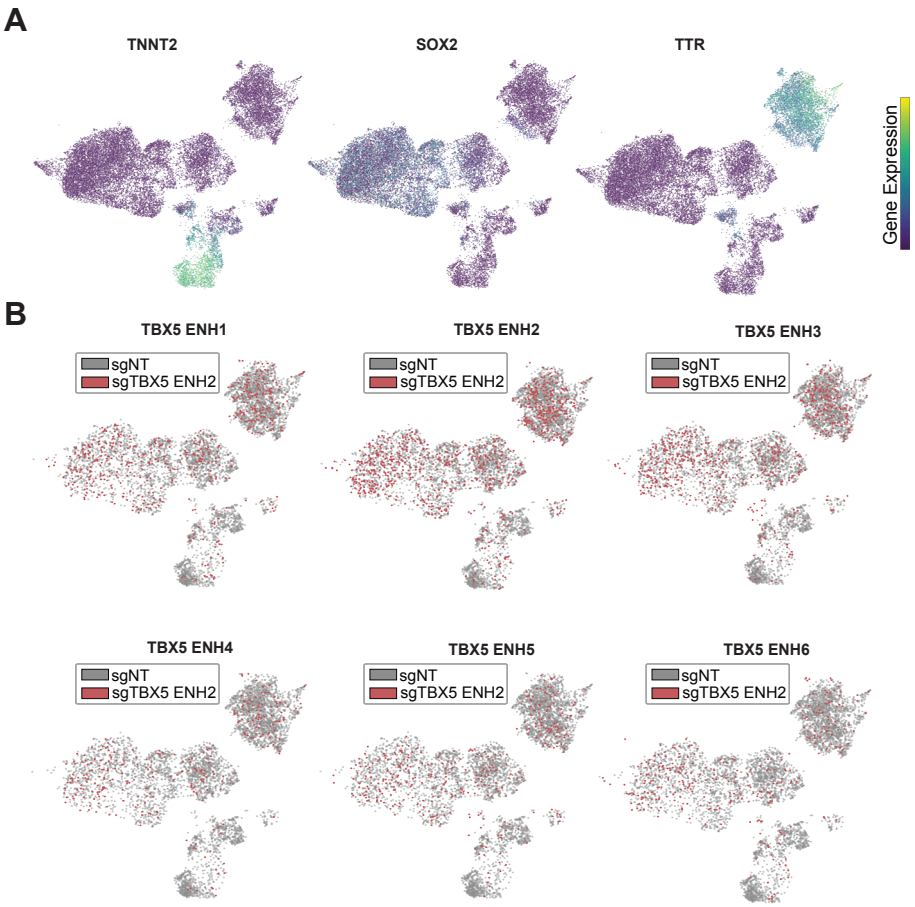

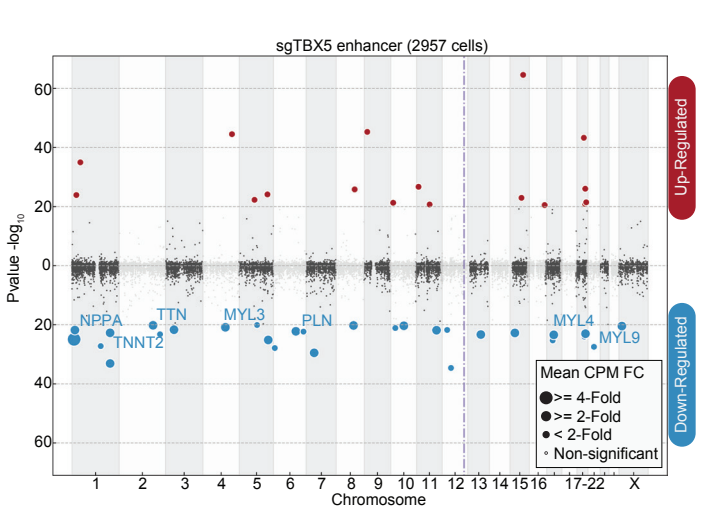

Figure S3: Focused screen marker expression and sgRNA distribution.

A. Feature plots of marker genes for neuronal (+SOX2), cardiomyocytes (+TNNT2), endoderm (+TTR).

B. Feature plots of cells receiving sgRNAs targeting TBX5 enhancers (red) or NT control (gray).

C. Differentially expressed genes in cells receiving sgRNAs targeting TBX5 enhancers. Please see description of Manhattan plot in Figure 2I.

Figure S4: TBX5 enhancer repression alters CM molecular signatures.

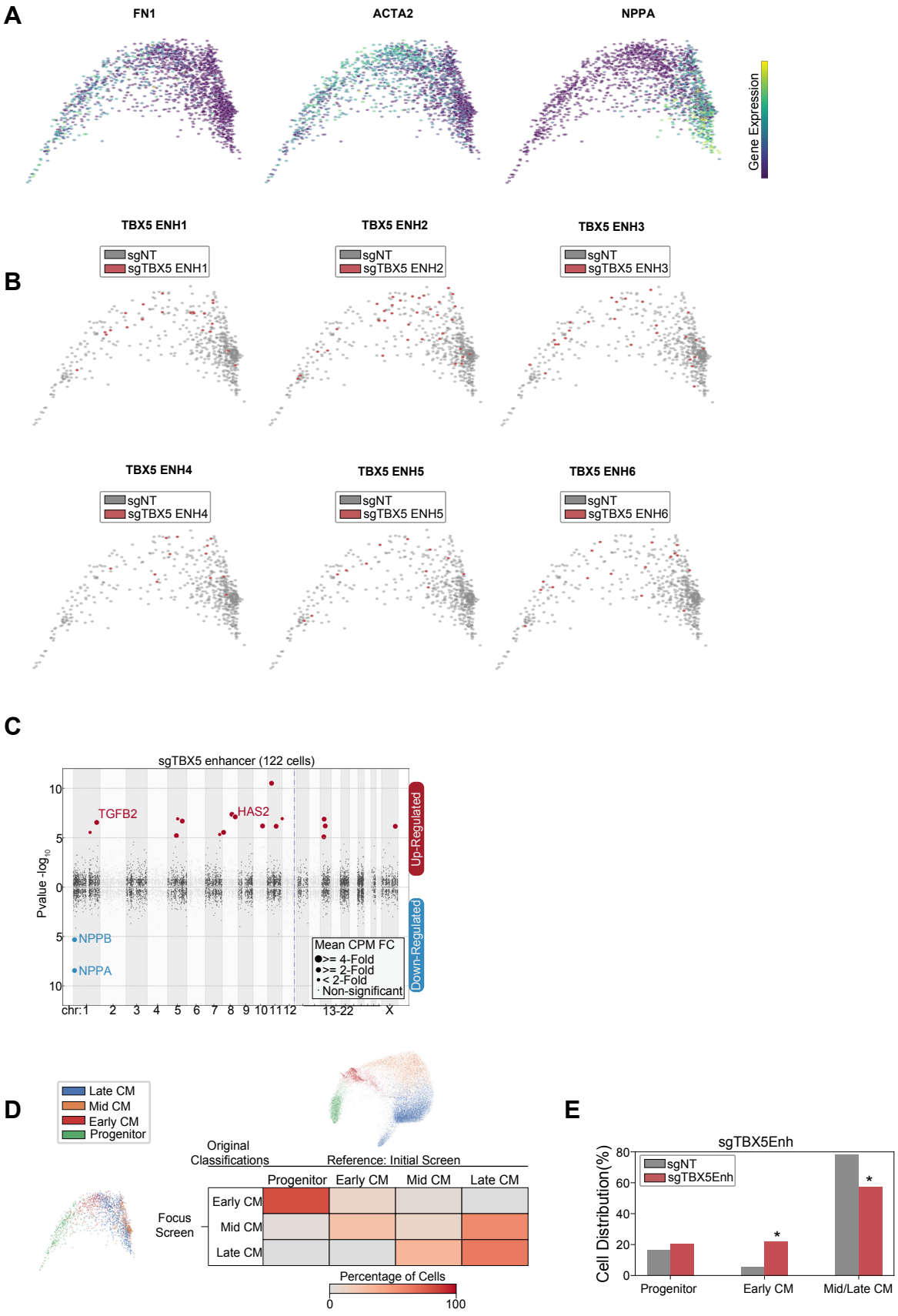

Figure S4: Focused screen CM subpopulation marker expression and sgRNA distribution.

A. PHATE visualization of CMs in the focused screen with 3 Louvain clusters.

B. Feature plots of cells receiving sgRNAs targeting TBX5 enhancers (red) or NT control (gray).

C. Differentially expressed genes in CM cells receiving sgRNAs targeting TBX5 Enhancers. Please see description of Manhattan plot in Figure 2I.

D. Reclustering of focused screen CM cells through cell label transfer using initial screen as reference.

E. Distribution of cells receiving sgRNAs targeting TBX5 Enhancers across label transferred CM subpopulations (* $p < 0.05$ by hypergeometric test).

Figure S5: TBX5 enhancer repression alters CM molecular signatures.

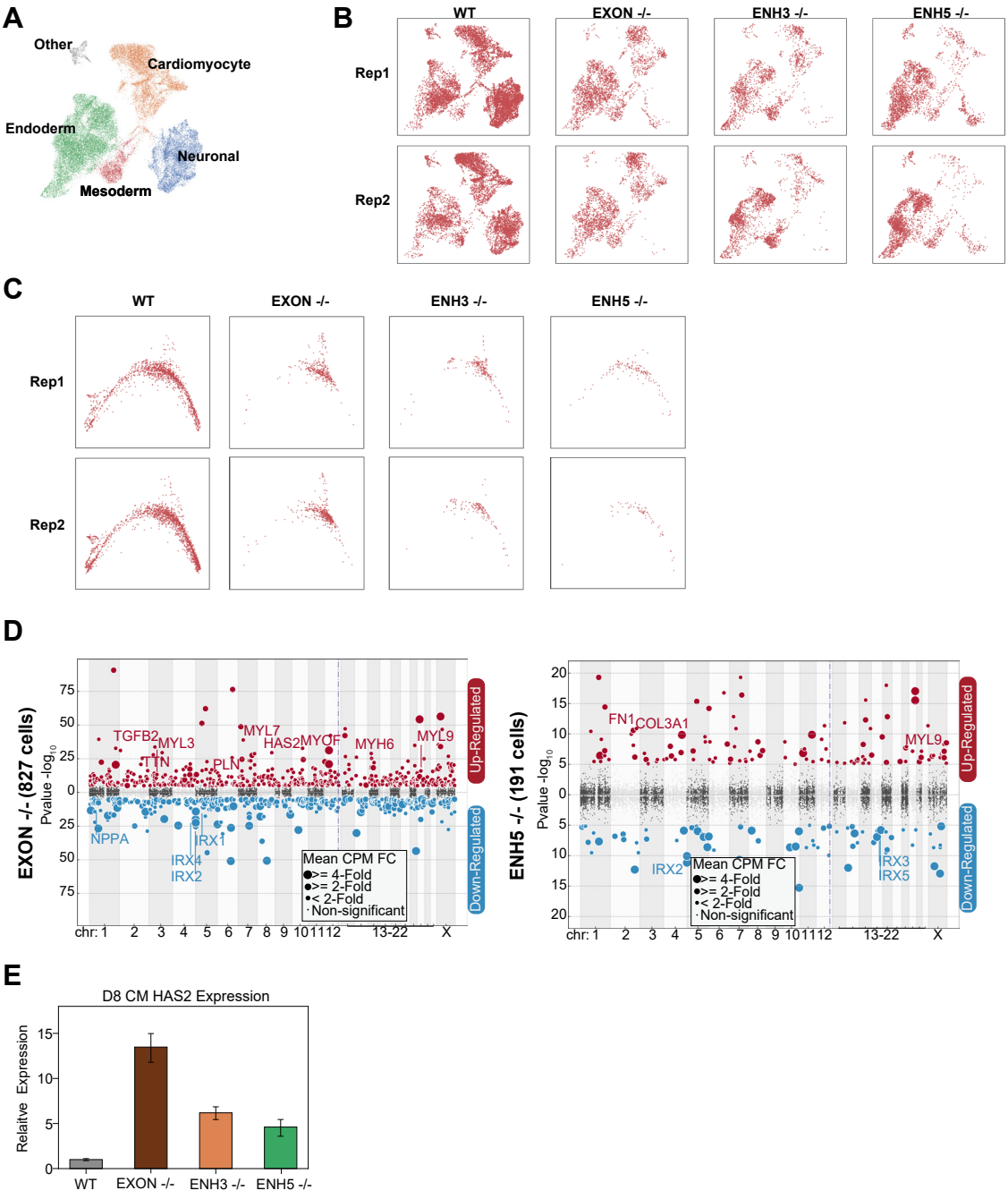

Figure S5: TBX5 enhancer knockout cell distribution.

A. UMAP visualization of H9-derived cells after 8 days of differentiation. 5 Louvain clusters indicated.

B. UMAP distribution of TBX5 exon KO and enhancer KO cells after CM differentiation. Shown are two replicate experiments per genotype.

C. PHATE distribution of TBX5 exon and enhancer KO CM differentiation replicate CM cells.

D. Differentially expressed genes in (left) TBX5 exon KO CM cells and (right) TBX5 enhancer 5 KO CM cells.

E. HAS2 transcript expression in exon and enhancer knockout cells after 8 days of CM differentiation. qPCR quantification normalized to reference gene (RPLP0) and then compared with WT cells.

Figure S6

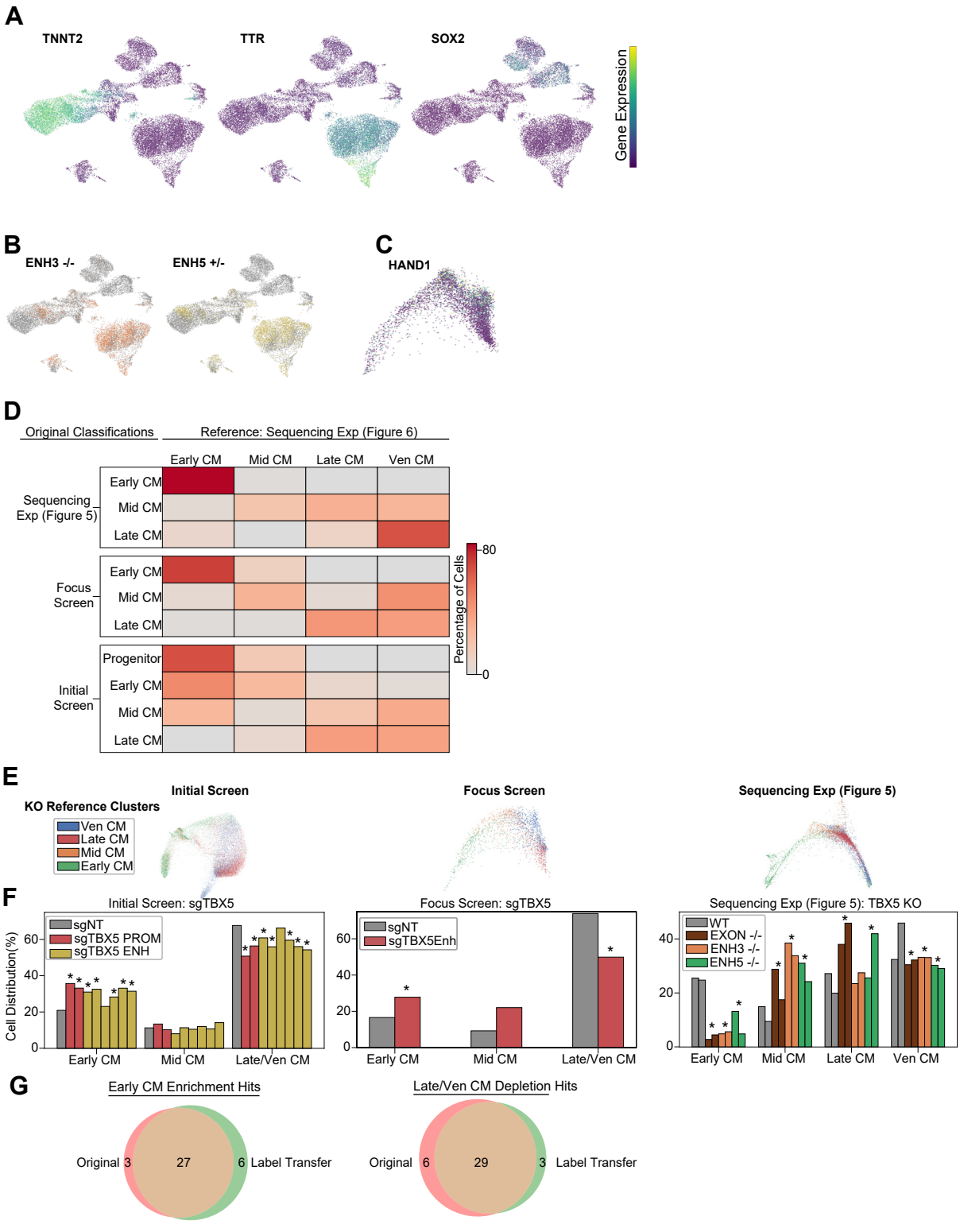

Figure S6: TBX5 heterozygous enhancer knockout validation.

A. Feature plots of marker genes for neuronal (+SOX2), cardiomyocytes (+TNNT2), endoderm (+TTR).

B. Feature plots of TBX5 enhancer 3 (orange), enhancer 5 (yellow) and WT (gray) CMs.

C. Feature plots of HAND1 expression.

D. Reclustering of CM cells from previous datasets through cell label transfer using sequencing exp (Figure 6) as reference.

E. PHATE distribution of CM cells clustered using 4 CM label transfer subpopulations.

F. Distribution of TBX5 enhancer perturbation cells across label transferred CM subpopulations (* $p < 0.05$ by hypergeometric test).

G. Overlap of early CM enriched (left) and late/ven CM depleted (right) hits from original and label transfer clustering of initial screen CMs.